Correct interpretation of nanofluid convective heat transfer

M.H. Buschmann[a,*], R. Azizian[b], T. Kempe[a], J.E. Juliá[c], R. Martínez-Cuenca[c], B. Sundén[d], Z. Wu[d], A. Seppälä[e], T. Ala-Nissila[f,g]

[a] *Institut für Luft- und Kältetechnik Dresden, 01309 Dresden, Germany*
[b] *Nuclear Science and Engineering Department, Massachusetts Institute of Technology, 77 Massachusetts Avenue, Cambridge, MA 02139, USA*
[c] *Departamento de Ingeniería Mecánica y Construcción, Universitat Jaume I, Castellón de la Plana 12071, Spain*
[d] *Department of Energy Sciences, Lund University, P.O. Box 118, Lund, SE 22100, Sweden*
[e] *Aalto University School of Engineering, Department of Mechanical Engineering, Thermodynamics and Combustion Technology, P.O. Box 14400, FI-00076 Aalto, Finland*
[f] *Department of Applied Physics and COMP Center of Excellence, Aalto University School of Science, P.O. Box 11000, FI-00076 Aalto, Espoo, Finland*
[g] *Departments of Mathematical Sciences and Physics, Loughborough University, Loughborough, Leicestershire LE11 3TU, United Kingdom*

ABSTRACT

Engineers and scientist have a long tradition in trying to improve the thermophysical properties of convective heat carriers such as water and transformer oil. Technological developments of the last decades allow the dispersion of particle of sizes ranging between 10 and 100 nm in these liquids. In a large number of recent studies the resulting nanofluids have been reported to display anomalously high increase of convective heat transfer. The present study compiles experiments from five independent research teams investigating convective heat transfer in nanofluid flow in pipes, pipe with inserted twisted tape, annular counter flow heat exchanger, and coil and plate heat exchangers. The results of all these experiments unequivocally confirm that Newtonian nanofluid flow can be consistently characterized by employing Nusselt number correlations obtained for single-phase heat transfer liquids such as water when the correct thermophysical properties of the nanofluid are utilized. It is also shown that the heat transfer enhancement provided by nanofluids equals the increase in the thermal conductivity of the nanofluid as compared to the base fluid independent of the nanoparticle concentration or material. These results demonstrate that no anomalous phenomena are involved in thermal conduction and forced convection based heat transfer of nanofluids. The experiments are theoretically supported by a fundamental similarity analysis of nanoparticle motion in nanofluid flow.

1. Introduction

Heat transfer is involved in countless industrial applications, including nuclear reactors, electronic devices, chemical reactors, engines, etc. Appropriate thermal management is a must in these systems to maintain reliability and prevent premature failure.

Consider electronic cooling area as an example. Technology advancements result in miniature micro-devices with higher packing density and therewith higher heat generation. This miniaturization leads to an increase in heat flux density that then needs to be dissipated, which is one of the most limiting barriers for technology advancement. Proper thermal management ensures reliable, high performance operation and maximizes the mean time between failures of microelectronic devices. There are a variety of solutions that can be implemented for cooling high power electronic devices using either air or liquid cooling. It has been shown that forced convection liquid cooling in microchannels (both single-phase and multi-phase flows) can provide a

solution for the cooling rate requirements of Microelectromechanical systems (MEMS) [1]. Clearly, the highest rate of heat dissipation can be attained by phase change. However, challenges associated with this solution such as high pressure drop, possible dryout, etc. have hampered the applicability of the phase change heat transfer in electronic cooling [1]. Although heat dissipation capability of single-phase forced convection is much smaller than multi-phase forced convection, it is more reliable and does not suffer from the aforementioned deficiencies related to multi-phase flow.

The effectiveness of single-phase convective heat transfer between a solid surface and a Newtonian fluid depends on fluid's thermophysical properties, its velocity, and system geometry. Hence, the generic functional form of all empirical correlations for prediction of single-phase forced convection heat transfer reads

$$Nu = f(GEO, Re, Pr) \qquad (1.1)$$

where Nu denotes the Nusselt number $(h\,l/k)$, GEO is some geometry

---

Nomenclature

A	surface area, m^2
a	thermal diffusivity, $a = k\,\rho^{-1}\,c_p^{-1}$, $m^2\,s^{-1}$
a, b	constant parameters
b_p	plate depth, m
c_p	specific heat capacity, $J\,kg^{-1}\,K^{-1}$
d	diameter, m
D	diffusion coefficient, $m^2\,s^{-1}$
D_c	coil diameter, m
De	Dean number, $De = \rho\,u\,d\,\mu^{-1}\,(d/D)^{0.5}$
f	friction factor
Fo	Fourier number, $Fo = \tau\,k\,d^{-1}\,\rho^{-1}\,c_p^{-1}$
G	heat exchanger conductance, $W\,K^{-1}$
GEO	geometrical parameter
h	heat transfer coefficient, $W\,m^{-2}\,K^{-1}$
HTC	heat transfer coefficient, $W\,m^{-2}\,K^{-1}$
I	rotational momentum of inertia
k	thermal conductivity, $W\,m^{-1}\,K^{-1}$
K_{Pe}, K_{Nu}	weighting factors
l	length, m
L	plate length, characteristic length, m
$LMTD$	logarithmic mean temperature
$\dot{m}$	mass flow rate, $kg\,s^{-1}$
n	number of turns in coil heat exchanger
Nu	local Nusselt number, $Nu = h\,d\,k^{-1}$
$\overline{Nu}$	Nusselt number averaged over device
Δp	pressure loss, Pa
p	coil pitch, m
Pe	Péclet number, $Pe = u\,d\,\rho\,c_p\,k^{-1}$
Pr	Prandtl number, $Pr = \mu\,c_p\,k^{-1}$
Q	heat amount, W
q	heat flux, $W\,m^{-2}$
Re	Reynolds number, $Re = \rho\,u\,d\,\mu^{-1}$
RH	ratio of heat transfer coefficient
RNu	ratio of Nusselt numbers
Sc	Schmidt number, $Sc = \nu\,D^{-1}$
T	temperature, K
U	overall heat transfer coefficient, $W\,m^{-2}\,K^{-1}$
u	velocity in streamwise direction, $m\,s^{-1}$
V	volume, m^3
v	velocity in wall normal direction, $m\,s^{-1}$
w	velocity in crossflow direction, $m\,s^{-1}$
x	streamwise/axial coordinate, m
y	wall normal/radial coordinate, m
z	crossflow coordinate, m

Greek symbols

ϕ	volumetric concentration of nanoparticles, %
Φ	surface enlargement ratio
φ	mass concentration of nanoparticles, %
δ	thickness (of wall etc.), mm
Δ	indicates relative differences of compared pairs, %
ζ	normalised pressure loss coefficient,
μ	dynamic viscosity, $kg\,m^{-1}\,s^{-1}$
ν	kinematic viscosity, $m^2\,s^{-1}$
Π	similarity number
ρ	density, $kg\,m^{-3}$
τ	time scale, s

Subscripts

a	annulus side
b	bulk
con	convection
B	Brownian motion
bf	base fluid
c	cold side
DB	Dittus-Boelter
dif	diffusion
e	equivalent
exp	experimental
h	hot side
H_2O	water
i	inner
in	inlet
nf	nanofluid
np	nanoparticle
o	outer
out	outlet
R	scale basis
ref	reference case
RePr	with respect to Reynolds and Prandtl number
s	sedimentation
T	thermophoresis
w	wall
proc	process

Superscripts

*	dimensional

Abbreviations

EMT	effective medium theory
ILK	Institut für Luft-und Kältetechnik Dresden
MIT	Massachusetts Institute of Technology
MWCNT	multi-walled carbon nanotube
NF	nanofluid
PdI	polydispersity index of the particle size distribution
PHE	plate heat exchanger
UJI	Universidad Jaume I

factor, Re is the Reynolds number ($\rho\,V\,l\,\mu^{-1}$) and Pr is the Prandtl number ($c_p\,\mu\,k^{-1}$).

The simplest way to increase the amount of heat transferred per unit volume is to enlarge the surface area where heat transfer takes place. However, this method leads to an undesirable increase in size and cost of unit operations. As a result, the most common practices currently are roughening the surface or increasing fluid velocity. While with the first technique the viscous sublayer is disturbed and a wall-normal velocity component is generated, the second approach aims to enhance flow dynamics by increasing the Reynolds number. All of these approaches usually result in greater pumping power. Practical applications show that these strategies have been already pushed to their limits.

To push the limits further, we are left with the option of changing the thermophysical properties of the working fluid which means changing the Prandtl number Pr and the Reynolds number Re. One obvious option is to replace the working fluid, which is not an easy solution, because in most of industrial applications there are many factors such as safety concerns that dictate the choice of the working fluid and replacement is not trivial. An alternative option is to modify the thermophysical properties of the original fluid by adding dispersed particles.

Dispersing particles with higher thermal conductivity than that of

the base fluid results in a higher overall thermal conductivity of the colloid. Challenges associated with this concept such as the settlement of micron or millimetre size particles, channel abrasion and high penalty in pressure drop have hindered their applicability in engineering systems. Through the development of nanotechnology, different methods have emerged to produce nanoparticles with sizes ranging from 10 to 100 nm of various shapes and material compositions. Such nanoparticles provide the advantage of a homogeneous dispersion that does not suffer from drawbacks associated with larger particles. The general expectation is also that the enhanced thermal conductivity of nanofluids leads to a higher heat transfer rate even at very low volume fractions $\phi \leq 1$ vol %. In many studies such behaviour has been described as *anomalous* enhancement of the thermal properties of dilute nanofluids.

Interest in implementing nanofluids as a heat transfer fluid was intensified after reports of high thermal conductivity of nanofluids in comparison to their pure fluid counterparts [2]. Nevertheless, thermal conductivity is just a part of the story. As it can be seen from the general form of the Nusselt number correlation (1.1) the heat transfer coefficient h is related to other thermophysical properties of the working fluid as well. Moreover, the general question arises if heat transfer of nanofluid flows can be predicted according to this correlation. The general assumption is that this is indeed possible as long as the effective thermophysical properties of the nanofluid are employed. This study critically assesses the validity of this assumption. For this purpose, five independent research groups have joined their efforts in investigating experimentally nanofluid heat transfer in lab scale as well as full scale heat transfer apparatus (such as various industrial heat exchangers).

In section two, we will present a brief introduction to the thermophysical properties of nanofluids and some basic arguments with respect to nanofluid flow. The third section discusses nanofluid flow from the point of similarity analyses. The following sections present the different experiments in detail. These are

- laminar and turbulent flow in a straight pipe with circular cross section (MIT, USA; UJI, Spain),
- laminar flow in straight pipe with circular cross section and inserted twisted tape (ILK Dresden, Germany),
- flow in a coil heat exchanger (University of Lund, Sweden),
- annular counter flow heat exchanger (Aalto University, Finland) and
- brazed heat exchanger (University of Lund, Sweden).

In the last section, the validity of our hypothesis will be evaluated based on our experimental results and theoretical considerations.

2. Thermophysical properties and some basic arguments

Higher effective thermal conductivity of nanofluids in comparison to their base fluid is the most advantageous feature of these colloids. Effective medium theory (EMT) can be used to estimate the transport properties of heterogeneous systems [1]. The linearized form of EMT, using a second order expansion, can be expressed as eq. (2.1)

$$\frac{k_{nf}}{k_{bf}} = 1 + K_k \phi + O(\phi^2).$$

(2.1)

Maxwell suggested $K_k = 3$ for dilute systems of spherical particles. The experimental results from the benchmark study of thermal conductivity measurement of nanofluids also confirm that for spherical particles eq. (2.1) with $K_k = 3$ can predict the experimental data with good accuracy [3].

There are several experimental studies that show either higher or lower values for thermal conductivity and propose correlations and mechanisms behind these observations. At this stage, thermal conductivity of nanofluids remains a controversial concept. Therefore, the best suggested practice to determine nanofluid thermal conductivity is

to experimentally measure it at various particle concentrations and temperatures. This strategy is employed in this study as well.

Evaluation of accurate viscosity correlations for nanofluids is a key for proper data validation. Similar to the thermal conductivity, despite several attempts, a satisfactory explanation for the increase of the viscosity in nanofluids is yet to be found. A general form of viscosity correlation as a function of concentration might be written [4] as

$$\frac{\mu_{nf}}{\mu_{bf}} = 1 + K_\mu \phi + O(\phi^2).$$

(2.2)

Einstein suggested $K_\mu = 2.5$ for dilute systems of spherical particles [4]. However, most of the reported experimental data show significantly higher values for K_μ. Therefore, the safest option seems to be again to experimentally determine the viscosity of the nanofluid at various particle concentrations and temperatures.

Density and heat capacity of nanofluids are predicted physically correct based on the mixture rule as

$$\rho_{nf} = \phi \rho_{np} + (1 - \phi)\rho_{bf},$$

(2.3)

and

$$c_{p,nf}\rho_{nf} = \phi \, c_{p,np}\rho_{np} + (1 - \phi)c_{p,bf}\rho_{bf}.$$

(2.4)

Equation (2.4) is based on the assumption of thermal equilibrium between the nanoparticles and the surrounding base fluid. A detailed derivation is given in Zhou et al. [5]. It was shown by several studies that eq. (2.4) represents experimental data with very good accuracy (e.g. O'Hanely et al. [6]).

Hereafter density and heat capacity of each nanofluid employed in this study are predicted based on eqs. (2.3) and (2.4). Thermal conductivity and viscosity were measured at various nanoparticle concentrations and temperatures. Only these data were used to predict heat transfer coefficient, non-dimensional parameters, etc.

The literature on nanofluid convective heat transfer shows controversial results. While a large number of publications support that the convective heat transfer enhancement goes beyond the prediction of established correlations of the form given by eq. (2.1) [7–9], others indicate that these correlations are in good agreement with their experimental results [10–13]. However, in studies that have concluded or assumed that nanofluids provide heat transfer enhancement with respect to their respective base fluids, the assessment of what constitutes an enhancement has not been conducted on the same basis. To give an example, the correlations for calculating Nu number contain Reynolds and Prandtl numbers in the form of $Re^m Pr^n$. Nanofluids generally have a higher thermal conductivity, density, viscosity and somewhat lower specific heat, which translates to higher values of Pr number. In many studies a comparison of Nu numbers for nanofluid and base fluid was carried out using identical Reynolds numbers, Re, which does not capture the whole picture. A true comparison should be based on experiments having identical $Re^m Pr^n$ values [14]. The reason is that only experiments which are fluid mechanically and thermodynamically similar should be compared. Comparison based on the Reynolds number alone ensures dynamical similarity but not thermodynamical one.

In studying nanofluids, the central question that needs to be answered is whether or not these suspensions are able to provide advantages in heat transfer applications over their pure liquid counterparts. In other words, do these special fluids behave in a fundamentally different way from homogenous single-phase Newtonian fluids? If nanofluids can be treated as homogeneous fluids, then traditional models and correlations developed for single-phase fluids are applicable, as long as appropriate loading and temperature dependent thermophysical properties of nanofluids are employed. In this study, an attempt is undertaken to validate this strategy.

In order to answer this question, we run various convective heat transfer experiments with different nanofluids. Then, thermophysical properties of nanofluids are measured/predicted as a function of

temperature and concentration. These thermophysical properties are used in traditional Nusselt number correlations developed for convective heat transfer of single-phase Newtonian fluid. In a final step the agreement between experimental and predicted data are analysed.

3. A few words on similarity analysis

The goal of this section is to discuss which physical phenomena are indeed relevant for experiments presented in the following chapters. The central question is

"Are nanofluid flows sufficiently described employing effective medium theory or do nanoparticles have their *own lives* and cause significant physical effects to a nanofluid flow which do not allow to see them as a single-phase flow?"

If nanofluids behave as ordinary ones, conventional Nusselt number and pressure loss correlations obtained investigating single-phase flow are applicable to nanofluid flows without restrictions. To answer this question a similarity analysis based on first principles is carried out. The goal is to unravel the forces affecting nanoparticles in a way that their behaviour is fluid mechanically and thermally different from their surroundings.

Effective medium theory demands that the base fluid and the nanoparticles are in thermodynamic equilibrium. Under real flow conditions a true equilibrium is not possible because fluid elements and nanoparticles are permanently exchanging energy, momentum and heat. The second law of thermodynamics however demands that this equilibrium is perpetually re-established [15]. Therewith, the above question reduces to whether the nanoparticles adjust sufficiently fast to the changes occurring in their surroundings or not. Based on this the following theorems are postulated.

Theorem #1. The characteristic time scale for a nanoparticle to adapt to the surrounding base fluid flow due to friction, must be significantly shorter than the time scale of the base fluid changing its velocity due to external influences.

Theorem #2. The characteristic time scale a nanoparticle needs to sediment in a heat transfer device with a certain characteristic length scale must be significantly longer than it takes to convect the nanoparticle through the device.

Theorem #3. The characteristic time scale for a nanoparticle to adapt to the surrounding base fluid temperature field due to thermal conduction must be significantly shorter than the time scale of the base fluid changing its temperature due to external influences.

Theorem #4. The time scales for a nanoparticle to diffuse due to temperature and concentration gradients must be significantly longer than the characteristic time scale of momentum diffusion.

Under these conditions the nanoparticles ideally follow the motion and the temperature changes of the surrounding base fluid. The presence of nanoparticles in the base fluid is accounted for by effective thermophysical properties – density, specific heat capacity, viscosity, thermal conductivity etc. – of the nanofluid. The validity of the above postulates and therewith the applicability of effective medium theory has to be proven for each experiment discussed in the following sections.

In addition to physical experiments and numerical simulations, similarity analysis belongs to the powerful tools to analyse fluid mechanical and thermodynamical problems. Their outcome – non-dimensional similarity numbers – are ratios of forces, fluxes etc. relevant to the problem under consideration. From this, their physical meaning follows which helps to understand the phenomena studied (Ruzicka, [16]). The relevant set of similarity numbers can either be obtained by non-dimensionalising the governing equations or by carrying out a dimensional analysis. For the complex non-isothermal flow situations

considered here, the first approach is preferred because less assumptions with respect to the relevant parameters have to be made.

The physical configuration considered with nanofluids consists of a Newtonian viscous base fluid interacting with mobile well-dispersed solid nanoparticles. The governing equations are the Navier-Stokes equations for the base fluid (see e.g. Prosperetti and Tryggavson [17]). In the following all bold printed variables indicate vectors.

$$\nabla \cdot \boldsymbol{u} = 0, \tag{3.1}$$

$$\rho_{bf}\left(\frac{\partial \boldsymbol{u}}{\partial t} + \nabla \cdot (\boldsymbol{uu})\right) = \nabla \cdot \boldsymbol{\tau}, \tag{3.2}$$

where $\boldsymbol{\tau}$ is the hydrodynamic stress tensor

$$\boldsymbol{\tau} = -p\boldsymbol{I} + \mu_{bf}(\nabla \boldsymbol{u} + (\nabla \boldsymbol{u})^T). \tag{3.3}$$

The balances for the translational momentum give the Lagrangian equations of motion of the particles,

$$m_{np}\frac{d\boldsymbol{u}_{np}}{dt} = \oint_{\Gamma} \boldsymbol{\tau} \cdot \boldsymbol{n} dS + V_{np}(\rho_{np} - \rho_{bf})\boldsymbol{g}, \tag{3.4}$$

and the angular momentum,

$$\frac{dI_{np}\,\boldsymbol{\omega_{np}}}{dt} = \oint_{\Gamma} \boldsymbol{r} \times (\boldsymbol{\tau} \cdot \boldsymbol{n}) dS. \tag{3.5}$$

The velocity at any point of the particle surface is

$$\boldsymbol{u}_{\Gamma} = \boldsymbol{u}_{np} + \omega_{np} \times \boldsymbol{r}. \tag{3.6}$$

The coupling of the continuous and the dispersed phase is carried out by the no-slip condition for the fluid at the particle surface, i.e.

$$\boldsymbol{u} = \boldsymbol{u}_{\Gamma}. \tag{3.7}$$

Note that the no-slip condition is usually valid for larger nanoparticles in liquids, but might be violated for small particles in gases. However, this depends on the Kundsen number which is the ratio of the mean free-path of the molecules to the characteristic length of the particles.

The temperature field inside a nanoparticle and the one of the surrounding base fluid are governed by the corresponding energy equations with the heat flux across the interface as the coupling condition. Due to the extraordinary smallness of nanoparticles, the thermal resistance of the nanoparticle/base fluid interface $R_s = 1/(h_{np}^* A_{np}^*)$ exceeds the thermal resistance of the volume of the nanoparticle $R_{th} = L_{np}^*/(k_{np}^* A_{np}^*)$. Here A_{np}^* denotes the nanoparticle surface and h_{np}^* the heat transfer coefficient at its surface. This yields a Biot number $Bi = R_{th}/R_s = L_{np}^* h_{np}^*/k_{np}^*$ much less than unity, which implies a homogenous temperature distribution inside the nanoparticle for a stationary flow situation and depends only on time (Herwig [64]). Note that the Biot number neither depends on any external force or the concentration of the nanoparticles. Consequently, it is not necessary to account for a spatially varying temperature inside the nanoparticle, but the thermodynamic state is sufficiently described by an average temperature (i.e. a single scalar value). Energy conservation is not affected in any case.

The above eqns. (3.1-3.7) constitute the governing equations for a general particulate flow in an Eulerian-Lagrangian description. Solving this system numerically is extremely challenging due to the tremendous number of nanoparticles which is of $O(10^{16}-10^{21})$ for practical applications. Another even more serious issue is the implementation of the moving boundary conditions at the nanoparticle surface into the Navier-Stokes equations.

The Eulerian-Eulerian approach are a more practical simulation framework at industrial scales. Here, the information on the locations and sizes of the individual particles is lost by virtue of the definition of a secondary continuous phase. Hence, the intense computations for the particles tracking is replaced by the resolution of the pressure and velocity fields of the second phase, as well as the spatial distribution of its

concentration. To sum up, the coupled transport of momentum and heat in a two-phase (liquid/solid) system needs the following equations for description [16].

1. continuity equation of liquid phase
2. momentum balance of liquid phase including momentum coupling to solid particle
3. thermal energy transport equation of liquid phase including thermal coupling to solid particles
4. continuity equation of solid phase
5. momentum balance of particles including momentum coupling to liquid phase
6. temperature transport equation of particles including thermal coupling to liquid phase

Let us note that the coupling of the two phases is a complex issue even for disperse flows. Here it is referred to a simplified homogeneous model, i.e. the velocity, pressure and temperature fields for each phase are shared. Which is valid for the case of Stokes numbers much smaller than unity. Then, the conservation of mass, momentum, and thermal energy are applied for the resulting binary mixture [18] which reads:

$$\frac{\partial u_i^*}{\partial x_i^*} = 0; \tag{3.8}$$

$$\rho_{nf}^* \frac{\partial u_i^*}{\partial \tau^*} + \rho_{nf}^* \frac{\partial u_i^* u_j^*}{\partial x_j^*} = \rho_{nf}^* g_j^* - \frac{\partial p^*}{\partial x_j^*} + \mu_{nf}^* \frac{\partial}{\partial x_j^*}\left(\frac{\partial u_i^*}{\partial x_j^*} + \frac{\partial u_j^*}{\partial x_i^*}\right); \tag{3.9}$$

$$\rho_{nf}^* c_{p,nf}^* \left(\frac{\partial T^*}{\partial \tau^*} + \frac{\partial u_j^* T^*}{\partial x_j^*}\right) = k_{nf}^* \frac{\partial^2 T^*}{\partial x_j^{*2}} + \rho_{np}^* c_{p,np}^*\left(D_B^* \frac{\partial \phi^*}{\partial x_j^*} + D_T^* \frac{1}{T^*} \frac{\partial T^*}{\partial x_j^*}\right)\frac{\partial T^*}{\partial x_j^*}. \tag{3.10}$$

Additionally a transport equation for the nanoparticle concentration is required [18,19]

$$\rho_{np}^* \left(\frac{\partial \phi^*}{\partial \tau^*} + \frac{\partial u_j^* \phi^*}{\partial x_j^*}\right) = \rho_{np}^* \frac{\partial}{\partial x_j^*}\left(D_B^* \frac{\partial \phi^*}{\partial x_j^*} + D_T^* \frac{1}{T^*} \frac{\partial T^*}{\partial x_j^*}\right). \tag{3.11}$$

In the above equations ρ, μ, k and c_p denote the thermophysical properties density, dynamic viscosity, thermal conductivity and heat capacity. The indices nf and np refer to the nanofluid and nanoparticle. Gravitational acceleration is denoted by g. The diffusion coefficients for Brownian motion and thermophoresis are indicated by D_B and D_T. The velocity components are indicated with u_i, temperature with T, pressure with p, the coordinates with x_i and the time with τ. The equations above employ dimensional quantities denoted by a superscript star.

Appendix A compiles the necessary non-dimensional variables. In these variables the index R indicates the reference values. Since we are interested in the deviation of convective heat transfer of a real nanofluid from the one assumed for a nanofluid with effective thermophysical properties normalisation of thermal conductivity, heat capacity, and density is carried out with the according differences between base fluid and nanoparticle thermophysical properties. In that sense, nanoparticles are seen as a perturbation of the homogeneity of the pure base fluid.

Heat capacity of solid nanoparticles is always lower than that of water which is the base fluid employed of the experiments discussed in the following sections. Therefore, to avoid negative similarity numbers, the heat capacity difference is multiplied by minus unity. Non-dimensionalisation of nanoparticle concentration ϕ follows straightforwardly from the definition of concentration.

Strictly speaking this approach is only correct if the governing equations are linear with respect to the thermophysical properties [20].

This is the case for temperature independent thermophysical properties only. While nanoparticle properties depend only weakly on temperature, base fluid properties show significant dependence. Therefore, the following analysis is restricted to a constant or only weakly changing temperature field.

In the first step, the non-dimensional variables are introduced into eqs. (3.8) – (3.11). Since friction is the only force that forces a nanoparticle to adapt to the surrounding flow, viscous scaling is carried out. For this purpose, eq. (3.9) is divided by the parameter group appearing in the viscous term. Under parameter group the combination of dimensional parameters – thermophysical properties, velocities etc. – appearing in each term after non-dimensionalisation is understood. The parameter groups found on the right hand side are employed to normalise all other equations. The normalisation yields

$$\frac{\partial u_i}{\partial x_i} = 0; \tag{3.12}$$

$$\Pi_1^{-1} \rho_{nf}\left(\frac{\partial u_i}{\partial \tau} + \frac{\partial u_i u_j}{\partial x_j}\right) = \Pi_2 \rho_{nf} g_i - \Pi_1^{-1}\frac{\partial p}{\partial x_j} + \mu_{nf}\frac{\partial}{\partial x_i}\left(\frac{\partial u_i}{\partial x_j} + \frac{\partial u_j}{\partial x_i}\right); \tag{3.13}$$

$$\rho_{nf} c_{p,nf}\left(\frac{\partial \theta}{\partial \tau} + \frac{\partial u_j \theta}{\partial x_i}\right) = k_{nf}\Pi_3 \frac{\partial^2 \theta}{\partial x_i^2} + \rho_{np} c_{p,np}\left(\Pi_4 D_B \frac{\partial \rho_{nf}}{\partial x_i} + \Pi_5 \frac{D_T}{\theta}\frac{\partial \theta}{\partial x_i}\right)\frac{\partial \theta}{\partial x_i}; \tag{3.14}$$

$$\rho_{np}\left(\frac{\partial \rho_{nf}}{\partial \tau} + \frac{\partial \rho_{nf} u_i}{\partial x_i}\right) = \frac{\partial}{\partial x_i}\left(\Pi_4 \rho_{np} D_B \frac{\partial \rho_{nf}}{\partial x_i} + \Pi_5 \frac{\rho_{np} D_T}{\theta}\frac{\partial \theta}{\partial x_i}\right). \tag{3.15}$$

The obtained similarity numbers Π_1 to Π_5 are compiled in Table 1. All parameter groups are written in the general form without specifying the characteristic length scale $L_{bf,R}^*$. Equations (3.14) and (3.15) provide two identical groups with Π_4 and Π_5. This is due to the fact that heat and nanoparticle concentrations diffuse equivalently under gradients of temperature and concentration.

The first parameter group Π_1 obtained from eq. (3.13) constitutes

Table 1
Similarity numbers obtained from eqs. (3.13) to (3.15) and (3.27).

Similarity numbers	eq.	Correlation	Short form
Stokes number Reynolds number	(3.13)	$\Pi_1^{-1} = \frac{u_{bf,R}^* L_{bf,R}^*}{\nu_{bf,R}^*}\left(\frac{\rho_{np,R}^*}{\rho_{bf,R}^*} - 1\right)$	$\Pi_1^{-1} = St - Re$
Reynolds number Archimedes number	(3.13)	$\Pi_2 = \frac{g_R^* L_{bf,R}^{*2}}{\nu_{bf,R}^* u_R^*}\left(\frac{\rho_{np,R}^*}{\rho_{bf,R}^*} - 1\right)$	$\Pi_2 = Ar\, Re^{-1}$
Péclet number weighting factor	(3.14)	$\Pi_3^{-1} = u_{bf,R}^* L_{bf,R}^* \frac{c_{p,bf,R}^* \rho_{bf,R}^*}{k_{bf,R}^*} * \left(\frac{\rho_{np,R}^*}{\rho_{bf,R}^*} - 1\right)\frac{\left(1 - c_{p,np,R}^*/c_{p,bf,R}^*\right)}{\left(k_{np,R}^*/k_{bf,R}^* - 1\right)}$	$\Pi_3^{-1} = Pe\, K_{Pe}$
Schmidt number Reynolds number	(3.14) (3.15)	$\Pi_4^{-1} = \frac{\nu_{bf,R}^*}{D_{B,R}^*}\frac{u_{bf,R}^* L_{bf,R}^*}{\nu_{bf,R}^*}$	$\Pi_4^{-1} = Sc_B\, Re$
Schmidt number Reynolds number	(3.14) (3.15)	$\Pi_5^{-1} = \frac{\nu_{bf,R}^*}{D_{T,R}^*}\frac{u_{bf,R}^* L_{bf,R}^*}{\nu_{bf,R}^*}$	$\Pi_5^{-1} = Sc_T\, Re$
Nusselt number weighting factor	(3.27)	$\Pi_6^{-1} = \frac{k_{bf,R}^* T_{bf,R}^*}{q_{w,R}^* L_{bf,R}^*}\left(\frac{k_{np,R}^*}{k_{bf,R}^*} - 1\right)$	$\Pi_6^{-1} = Nu^{-1} K_{Nu}$

two similarity numbers, namely the Stokes number St and the Reynolds number Re. That the Stokes number appears besides the Reynolds number is due to the chosen normalisation utilizing the difference between the densities of nanoparticles and base fluid. In the idealised case of massless nanoparticles not able to transport inner energy or conduct heat, nanoparticle density equals zero and the Stokes number becomes identically zero. Classical scaling based solely on Re remains. As an aside we note that the Dean number – as employed in Sec. 4.3 for coil heat exchanger – appears instead of the Stokes number when eq. (3.13) is normalised with the difference between the inner diameter of the coiled pipe and the diameter of the coil.

The Stokes number is the ratio of time scales addressed in Theorem #1.

$$St = \frac{u_{bf,R}^* L_{bf,R}^*}{\nu_{bf,R}^*} \frac{\rho_{np,R}^*}{\rho_{nf,R}^*}; \quad St = \frac{\tau_{np,\nu}^*}{\tau_{nf,con}^*};$$
$$\tau_{np,\nu}^* = \frac{L_{bf,R}^{*2}}{\nu_{bf,R}^*} \frac{\rho_{np,R}^*}{\rho_{bf,R}^*}; \qquad \tau_{bf,con}^* = \frac{L_{bf,R}^*}{u_{bf,R}^*}. \tag{3.16}$$

The characteristic time scale of the nanoparticles $\tau_{np,\nu}^*$ is the viscous time scale $\tau_{bf,\nu}^* = L_{bf,R}^{*2}/\nu_{bf,R}^*$ of the base fluid multiplied by the density ratio. The characteristic convective time scale of the base fluid is denoted by $\tau_{bf,con}^*$. Since the density of the nanoparticles is always larger than that one of water which is the base fluid employed here, the viscous time scale allowing the nanoparticle to adapt to the surrounding flow is increased. However, as long as $St \ll 1$ the nanoparticles follow the local base fluid flow with negligible time lag. Moreover, in such a situation nanoparticles move coplanar to any wall (heat exchanger plate etc.) since the wall-normal velocity component is nearly zero there. Therefore, one can hypothesize that no additional heat transfer, related to nanoparticle bouncing or re-bouncing due to inertia, occurs at the wall of a heat transfer device.

The second parameter group Π_2 found from eq. (3.13) provides the Archimedes number Ar. The Archimedes number corresponds to the Galileo number $Ga = g_R^* L_{bf,R}^{*3}/\nu_{bf,R}^{*2}$ – the ratio between gravitational and viscous forces – weighted by the density ratio:

$$Ar \, Re^{-1} = \frac{g_R^* L_{bf,R}^{*2}}{\nu_{bf,R}^* u_{bf,R}^*} \frac{\rho_{np,R}^*}{\rho_{bf,R}^*}; \quad Ar \, Re^{-1} = \frac{\tau_{np,\nu}^*}{\tau_g^*};$$
$$\tau_{np,\nu}^* = \frac{L_{bf,R}^{*2}}{\nu_{bf,R}^*} \frac{\rho_{np,R}^*}{\rho_{bf,R}^*}; \qquad \tau_g^* = \frac{u_{bf,R}^*}{g_R^*}. \tag{3.17}$$

The parameter group Π_2 is Stokes' law normalised with the sedimentation rate of the nanoparticles. Thus it also represents the buoyancy of the nanoparticles. In case of non-zero mean velocity the particles are convected with the flow. Therefore, it seems plausible to address Theorem #2 not by predicting the Archimedes number but rather the ratio of the time it takes for a nanoparticle to sediment inside the device $\tau_{np,s}^*$ to the characteristic time scale of the device $\tau_{bf,con}^*$. The characteristic length scale is then that one of the device (pipe diameter, channel height etc.). Note that the Stokes number and the Archimedes number provide two independent statements which cannot be combined.

$$\Pi_\tau = \frac{\tau_{np,s}^*}{\tau_{bf,con}^*}; \quad \tau_{np,s}^* = \frac{9\,\mu_{bf,R}^* L_{bf,R}^*}{2\,g_R^* (d_{np}^*/2)^2 (\rho_{np,R}^* - \rho_{bf,R}^*)};$$
$$\tau_{bf,con}^* = \frac{L_{bf,R}^*}{u_{bf,R}^*}. \tag{3.18}$$

Conservation of thermal energy (3.14) indicates with Π_3 a combination of the well-known Péclet number Pe and the *weighting factor* K_{Pe}. The Péclet number can be represented as the product of Reynolds and Prandtl number. It relates convective and diffusive transport rates of the base fluid. With the momentum equation (3.12) the Reynolds number in its modified form the Stokes number is already discussed. Because Stokes and Péclet number are completely independent the weighting factor K_{Pe} is seen in conjunction with the Péclet number alone. It modifies the Péclet number with respect to the ability of the

nanoparticles to carry and to conduct heat and therewith to affect the diffusive transport of heat within the base fluid. Note that K_{Pe} depends only on the thermophysical properties of the nanoparticles. In the idealised case of massless nanoparticles not able to transport inner energy or conduct heat the weighting factor becomes unity and the classical scaling with Pe alone remains.

Péclet number can be understood as a similarity number equivalent to the ratio of the characteristic time scales of the base fluids momentum diffusion $\tau_{bf,dif}^*$ and it's convective transport $\tau_{bf,con}^*$.

$$Pe = u_{bf,R}^* L_{bf,R}^* \frac{\rho_{bf,R}^* c_{p,bf,R}^*}{k_{bf,R}^*}; \quad Pe = \frac{\tau_{bf,dif}^*}{\tau_{bf,con}^*};$$
$$\tau_{bf,dif}^* = L_{bf,R}^{*2} \frac{\rho_{bf,R}^* c_{p,bf,R}^*}{k_{bf,R}^*}; \qquad \tau_{bf,con}^* = \frac{L_{bf,R}^*}{u_{bf,R}^*}. \tag{3.19}$$

Nanoparticles are solid and their density is always larger than that of water. Moreover, due to this solidity their specific heat capacity is in any case lower than that of water. Thermal conductivities of nanoparticle materials range from slightly higher than that of water (e.g. silica [21]) to several orders of magnitude larger than that of water (e.g. CNT, diamond [21]). Based on these considerations the weighting factor

$$K_{Pe} = \left(\frac{\rho_{np,R}^*}{\rho_{bf,R}^*} - 1 \right) \frac{(1 - c_{p,np,R}^*/c_{p,bf,R}^*)}{(k_{np,R}^*/k_{bf,R}^* - 1)} \tag{3.20}$$

may take values between zero and unity and will reduce the Péclet number in the most cases. This indicates enhanced heat diffusion, which is indeed the motivation behind adding nanoparticles to a base fluid. However, it should be noted that this effect is significant only in the immediate vicinity of the nanoparticles and thus restricted to very small length scales.

Unfortunately, the Péclet number is not directly related to Theorem #3. The reason is simply that no time scale for heat transport inside the nanoparticles has appeared so far. This deficit is removed by analysing the heat equation

$$\frac{\partial T_{np}^*}{\partial \tau^*} = a_{np}^* \nabla^2 T_{np}^*; \quad a_{np}^* = \frac{k_{np}^*}{\rho_{np}^* c_{p,np}^*} \tag{3.21}$$

for the nanoparticle interior. Here a_{np}^* denotes the thermal diffusivity of the nanoparticle material and T_{np}^* is the temperature inside the nanoparticle. Non-dimensionalising eq. (3.21) according to Appendix B results in

$$\frac{\partial \Theta}{\partial \tau} = Fo \, a_{np} \nabla^2 \Theta \tag{3.22}$$

with the non-dimensional group appearing on the right hand side of eq. (3.22) being the Fourier number Fo defined in eq. (3.23). The Fourier number is the non-dimensionalised time of an instantaneous heat transfer problem. However, it can be also understood as the ratio of a certain process time τ_{proc}^* imposed on the nanoparticle and the thermal equilibration time $\tau_{np,eq}^*$ of this nanoparticle.

$$Fo = \frac{\tau_{proc}^*}{L_{np,R}^{*2}} \frac{k_{np,R}^*}{\rho_{np,R}^* c_{p,np,R}^*}; \quad Fo = \frac{\tau_{proc}^*}{\tau_{np,eq}^*};$$
$$\tau_{np,eq}^* = L_{np,R}^{*2} \frac{\rho_{np,R}^* c_{p,np,R}^*}{k_{np,R}^*}. \tag{3.23}$$

Utilizing the time scale characterising the base fluid $\tau_{bf,con}^* = L_{bf,R}^*/u_R^*$ (eq. (3.16)) as the process time τ_{proc}^* the time needed for heating or cooling a nanoparticle $\tau_{np,eq}^*$ due to temperature changes of the surrounding base fluid becomes comparable with the convective time scale of this base fluid.

$$Fo = \frac{L_{bf,R}^*}{u_{bf,R}^*} \bigg/ L_{np,R}^{*2} \frac{\rho_{np,R}^* c_{p,np,R}^*}{k_{np,R}^*}. \tag{3.24}$$

The characteristic length scale of the nanoparticle $L_{np,R}^*$ follows from dividing its volume by its surface. For a spherical nanoparticle it then

follows that $L_{np,R}^* = d_{np}^*/6$, where d_{np}^* denotes the nanoparticle diameter. The Fourier number as given with eq. (3.24) is basically the ratio of time scales addressed with Theorem #3.

The two other similarity numbers − Π_4 and Π_5 – appearing in (3.14) and (3.15) are products of the Reynolds number and the Schmidt number. Schmidt number is the ratio of momentum diffusion to mass diffusivity either due to Brownian motion or due to thermophoretic diffusion. The relevant time scales for these processes are addressed in Theorem #4. They read:

$$Sc_{B,T} = \frac{\nu_{bf,R}^*}{D_{B,T,R}^*}; \quad Sc_{B,T} = \frac{\tau_{D,B,T}^*}{\tau_{bf,\nu}^*};$$

$$\tau_{D,B,T}^* = \frac{L_{bf,R}^{*2}}{D_{B,T,R}^*}; \quad \tau_{bf,\nu}^* = \frac{L_{bf,R}^{*2}}{\nu_{bf,R}^*}. \tag{3.25}$$

Large Schmidt numbers – $Sc_B \gg 1$ and/or $Sc_T \gg 1$ – indicate that momentum diffusion is much faster than mass diffusion caused by concentration or temperature gradients, respectively.

The Nusselt number – the non-dimensional heat flux q_w^* – follows straightforwardly from Fourier's law of heat conduction written at the wall (index w).

$$q_w^* = -k_{bf}^* \left(\frac{\partial T^*}{\partial x_j^*} \right)_w; \tag{3.26}$$

$$\Pi_6 \, q_w = -k_{bf} \left(\frac{\partial T}{\partial x_j} \right)_w. \tag{3.27}$$

The similarity number Π_6 is a product of the Nusselt number and a weighting factor. The weighting factor K_{Nu} reads:

$$K_{Nu} = \left(\frac{k_{np,R}^*}{k_{bf,R}^*} - 1 \right). \tag{3.28}$$

This weighting factor is basically the first term of K_{Pe}, eq. (3.20), and ranges between unity and $O(10^3)$. Interpreting the Nusselt number as the ratio between the actual convective heat transfer and an imaginary heat transfer solely based on conduction, the weighting factor K_{Nu} indicates the expected increase of the actual heat transfer due to the presence of nanoparticles. An overwhelming majority of measurements of effective thermal conductivity shows that the increase achieved is significantly less than the ratio k_{np}/k_{bf} would suggest. This is due to the relatively low volume fraction occupied by the nanoparticles and their uniform dispersion. Theoretically it is possible that nanoparticles order in chains parallel or perpendicular to the direction of the heat flux (Eapen et al., [21]). In the first case, assuming that the thermal contact resistance between nanoparticles is negligible, a band of nanoparticles having indeed the thermal conductivity of the nanoparticle material would occur. But this band would be very narrow due to the low volume fraction occupied by nanoparticles so that even in this very unlikely scenario the increase of thermal conduction would be very small.

The analysis above indicates the following Nusselt number correlation for the nanofluid flow.

$$Nu = f(GEO, \, Re_{nf}, \, Pr_{nf}, \, St, \, \Pi_\tau, \, K_{Pe}, \, K_{Nu}, \, Fo, \, Sc_B, \, Sc_T). \tag{3.29}$$

In eq. (3.29) GEO denotes any parameters related to the specific geometry of the heat transfer device. The Reynolds number Re is built with the characteristic length scale $L_{bf,R}^*$ of the device and the characteristic velocity of the flow and the kinematic viscosity of nanofluid.

There is no doubt that as in any single-phase flow, the Reynolds number based on the physical parameters of the device and the Prandtl number based on base fluid's thermophysical properties are relevant for nanofluid flow. All other non-dimensional groups appearing in eq. (3.29) have to be calculated for the specific experimental conditions and analysed with respect to the theorems given at the beginning of this section. For the experiments discussed here these values are compiled in Table 2. An exception are the experiments carried out with CNT or MWCNT. Due to the large length of these particles (up to 1 μm) the results e.g. for the Stokes number are misleading. Moreover, heat capacity and thermal conductivity of these materials are either not available from the literature or they are unrealistically high.

Table 2 indicates that the Stokes number is in most cases two orders of magnitude smaller than unity. Therefore, the condition in Theorem #1 is satisfied. Due to their smallness and the viscous force nanoparticles follow the surrounding base fluid without any time lag.

The characteristic time a nanoparticle needs to sediment within the heat transfer devices, as Π_τ indicates, is at least six orders of magnitude larger than it takes to transport it once through the device. Hence, sedimentation and buoyancy as addressed in Theorem #2 should not play a significant role with respect to convective heat transfer.

As already mentioned, the weighting factors K_{Pe} and K_{Nu} indicate the influence of nanoparticles ability to conduct and carry heat. Even if these factors are not unity, the effects they describe are weak due to the small volume fraction occupied by the nanoparticles and the well-dispersed character of the nanofluids employed. Therefore, local perturbation of the temperature field by nanoparticles as addressed by Theorem #3 is seen to be small.

Moreover, let's assume that a nanoparticle's characteristic length is of the order of $O(10^{-8}, 10^{-7})$ (10 nm, 100 nm) and its thermophysical properties such as density, specific heat capacity and thermal conductivity are of the order of $O(10^4)$, $O(10^2)$ and $O(10^2)$, respectively. For the characteristic length scale of a certain heat transfer apparatus a characteristic length $L_{bf,R}^*$ of the order of $O(10^0)$ and a characteristic velocity $O(10^1)$ are considered. All together this leads to the conclusion that the Fourier number Fo is of the order of $O(10^9)$ to $O(10^{11})$. The thermal equilibration time $\tau_{np,eq}^*$ of the nanoparticle is therefore

Table 2
Predicted similarity numbers for experiments.

Experiment	St	$\Pi_\tau \times 10^{-7}$	K_{Pe}	K_{Nu}	$Sc_B \times 10^{-4}$	$Sc_T \times 10^{-6}$
laminar entrance pipe flow [10]						
Al_2O_3	0.01, 0.23	1.18, 23.33	0.04	56.65	6.08	3.81
ZrO_2	0.02, 0.33	0.70, 14.66	1.84	2.29	6.08	0.68
turbulent pipe flow [24]						
SiO_2	0.06, 1.56	0.24, 6.33	1.05	1.30	22.44	0.33, 1.65
Al_2O_3	0.06, 1.65	0.34, 8.95	0.04	56.65	15.44	4.57, 22.87
laminar pipe flow with twisted tape [39]						
TiO_2	0.02, 0.06	0.34, 1.03	0.15	18.27	10.34	0.82, 1.63
coil heat exchanger [49]						
Al_2O_3	0.01, 0.19	1.74, 38.19	0.04	56.65	4.86	8.05–114.36
annual counter flow heat exchanger [52]						
SiO_2	0.01–0.14	2.24, 35.15	1.05	1.30	5.72–7.05	0.91–1.83
Al_2O_3	0.00–0.03	42.57, 438.78	0.04	56.65	1.22	22.87–45.74
plate heat exchanger [61]						
Al_2O_3	0.01–0.2	1.74–38.19	0.04	56.65	4.86	8.05–114.36

significantly smaller than the characteristic inertia dominated time scale of the base fluid. This finding is in agreement with the conclusions drawn from the discussion of the Biot number made above. A nanoparticle has a nearly constant inner temperature and follows practically immediately the changes of the temperature field of the surrounding base fluid. A transport of thermal energy by nanoparticles in a *container-like-mode* over long distances seems therefore not possible.

The values predicted for Sc_B range between $O(10^4)$ and $O(10^5)$ and for Sc_T between $O(10^5)$ and $O(10^7)$. Therefore, the nanoparticle Schmidt numbers are significantly larger than unity and momentum transport dominates nanoparticle motion which satisfies Theorem #4.

To summarize it is very unlikely that effects related to the dynamics of the nanoparticles affect heat transfer significantly in the experiments. Effects such as separation of nanoparticle motion from the motion of the surrounding base fluid due to nanoparticle inertia, thermophoresis due to temperature gradients, and other factors occur in all nanofluid flows but they are of minor importance for the experiments presented here. The consequence is that effective medium theory can be employed and standard Nusselt number correlation of the form

$$Nu = f(GEO, \ Re_{nf}, \ Pr_{nf}) \tag{3.30}$$

obtained from single-phase should be applicable.

4. Experiments

4.1. Laminar and turbulent flow in a straight pipe with circular cross section and constant heat flux (MIT, USA; UJI, Spain)

Heat transfer characteristics of nanofluids have been studied at MIT and UJI with the goal of evaluating their benefits for and applicability to heat transfer systems, especially for nuclear power systems. Various studies have been done on flow boiling [22] and pool boiling [23] as well as single phase characterization of nanofluids [10–12,23]. Overview of the single phase heat transfer (laminar and turbulent) is related to this work and presented here. To study single phase heat transfer of nanofluids the central question that needs to be answered is whether or not nanofluids are able to provide advantages in heat transfer applications over their pure liquid counterparts. The other important question to be answered is whether or not nanofluids behave in a fundamentally different way from homogenous fluids.

As we have already stated the literature on nanofluid convective heat transfer experiments shows controversial results. While a large number of publications support that the convective heat transfer enhancement goes beyond the prediction of established correlations [7–9,19,24–29], others indicate that the established correlations can predict their experimental data with a good accuracy [10,13,23,27,30–34]. However, in studies that have concluded or assumed that nanofluids provide heat transfer enhancement with respect to their respective base fluids, assessment of what constitutes an enhancement has not been determined on the same basis. According to the established correlations for laminar and turbulent convective heat transfer, the heat transfer coefficient (HTC) depends on the thermophysical properties, flow parameters and geometry. Therefore, an increased HTC may simply reflect the changes in the thermal physical properties of the nanofluid being tested, while the models and correlations developed for simple fluids still apply.

Interestingly, in convective heat transfer experiments conducted at MIT [10–12] with alumina-water and zirconia-water as well as magnetite-water nanofluids, it was shown that if the measured temperature- and loading-dependent thermo-physical properties are used in calculating the dimensionless numbers (i.e. Reynolds, Prandtl and Nusselt numbers), the existing correlations accurately reproduce the convective heat transfer and viscous pressure loss behaviour in tubes within measurement uncertainties. The same observation was made at UJI [24] with silica-water, alumina-water and CNT-water nanofluids. These observations are interesting because they show that there is no
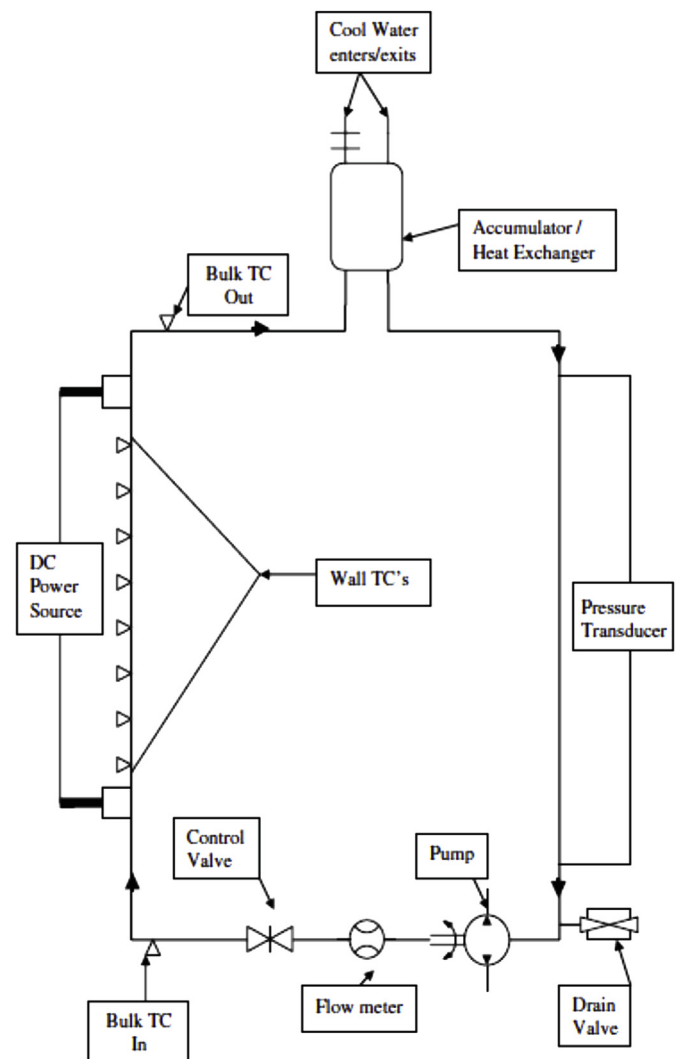

Fig. 1. Schematic of the laminar flow convective heat transfer loop at MIT [10].

nanoparticle-specific heat transfer mechanisms that make nanofluids behave in a fundamentally different way from homogenous fluids and all the nanofluids studied at MIT and UJI can be treated as homogeneous mixtures, as such the HTC enhancement is not abnormal, but due to the different mixture properties of the nanofluids.

4.1.1. Description of the test rig

4.1.1.1. Laminar pipe flow at MIT. Laminar convective heat transfer and viscous pressure loss were investigated for alumina–water, zirconia–water and magnetite-water nanofluids in a flow loop with a vertical heated tube. A schematic of the experimental test rig used for laminar convective heat transfer measurements of nanofluids at MIT is shown in Fig. 1 [10]. The experimental loop was designed for convective heat transfer in the laminar flow domain. It was constructed with circular stainless steel tubing, and the fluid (either DI-water or nanofluid) was pumped throughout the system by a miniature gear pump (McMaster-Carr). The volumetric flow rate was measured with a FTB9504 Omega flow turbine meter (which has an accuracy of 0.50% in the range of 0.80–16.7 cm³/s). The flow meter was positioned just after the pump discharge. The test section was a vertical heated section of the loop with a stainless steel tube with an inner diameter (ID) of 4.50 mm, outer diameter (OD) of 6.40 mm, and length of 1.01 m. The test section had eight sheathed and electrically insulated T-type thermocouples soldered onto the outer wall of the tubing along axial locations of the test section ($z = 5, 16, 30, 44, 58, 89$

and 100 cm) from inlet of the heated section. Two similar T-type thermocouples were inserted into the flow channel before and after the test section to measure the bulk fluid temperatures. These thermocouples and the flow meter provided the data to determine the thermal power of the experimental loop. The test section used in the experiment was a resistively heated by a DC power supply (Sorensen DCR 20–125). After being heated the fluid was cooled using a chiller that provided flow to a coil placed in the accumulator. After the test fluid was cooled, it ran through a 1.45 m long and 5.8 mm ID vertical isothermal section where the pressure loss was measured by a pressure transducer (Omega PX 154-001DI, with an accuracy of 1%).

4.1.1.2. Turbulent pipe flow at MIT. Similar to the laminar flow tests, the convective heat transfer coefficient and viscous pressure loss were experimentally measured for alumina–water and zirconia–water nanofluids under fully developed turbulent flow conditions. A separate test rig was built for this purpose (Fig. 2). The test section was made of a smooth horizontal stainless steel tube, with 3 m length (because of the length of the test section the entry region effect on heat transfer is negligible), 12.7 mm outside diameter (OD) and 9.4 mm inner diameter (ID) heated by a DC power supply from Lambda America, providing a maximum power of 24 kW. The wall temperature was read by fourteen T-type thermocouples, which are axially separated by 0.2 m. The inner wall temperature was calculated assuming radial heat conduction within the tube wall. Similar to the laminar flow loop, there were also two T-type thermocouples submerged in the flow channel at the inlet and outlet of the heated section to measure the bulk temperature of the fluid. The flow is provided by a 1 HP Berkeley SS1XS1-1 pump with a frequency speed controller. The flow is measured by a similar flow meter as of the laminar flow loop with ± 0.5% accuracy. The heat was removed by a stainless steel shell-and-tube heat exchanger [12].

It is also important to mention that there is a potential for mixed convection effects in a horizontal test section. The large film temperature gradient as a result of high heat fluxes could give rise to buoyant mixing and radial test section temperature variation. The amount of buoyancy contribution to the overall flow is determined through a ratio of Grashof and Reynolds number as Gr/Re^2. If this ratio is greater than 0.1 then the effect of buoyancy will begin to alter the flow. This value was calculated to be less than 0.01 (for various test conditions in this study) and thus should not alter the flow under our experimental
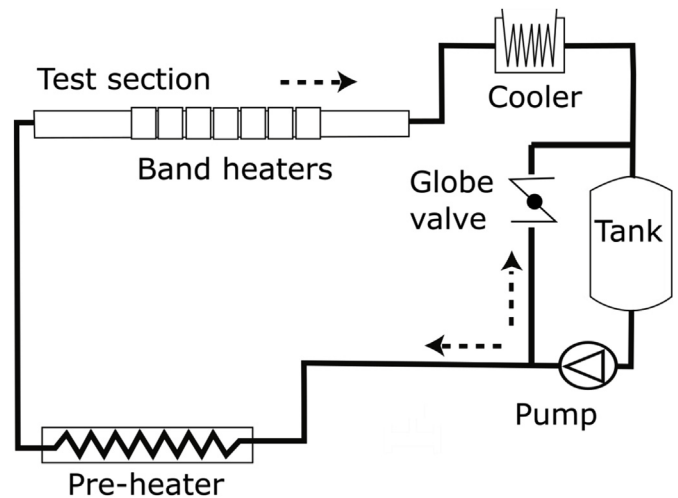

Fig. 3. Schematic of the turbulent flow convective heat transfer loop at UJI [24].

conditions [35].

The viscous pressure loss was also measured over the isothermal section of the flow loop for the same length. The pressure loss was measured directly by a differential pressure transducer, Omega PX293-030D5V, operating over a range of 0–207 kPa with accuracy to within 0.5%, as calibrated by the manufacturer.

4.1.1.3. Turbulent pipe flow at UJI. Experiments under fully-developed turbulent flow in a horizontal pipe were carried out at UJI. The schematic of a full loop is depicted in Fig. 3. The test section consisted of a round aluminum pipe with an inner diameter of 31.2 mm and 3.6 mm thickness. The heated length of the pipe was 1,000 mm, and an unheated length of 500 mm was left both before and after the test section. This is to ensure fully-developed flow condition as well as to avoid disturbance of the flow in a heated section.

Eighteen band heaters were placed all along the test section in order to provide a uniform heat flux up to 107 kW/m^2 across the test section. Both heated and unheated pipe sections were insulated employing Morgan Superwool® Fibre 607 (10 mm thickness). The working
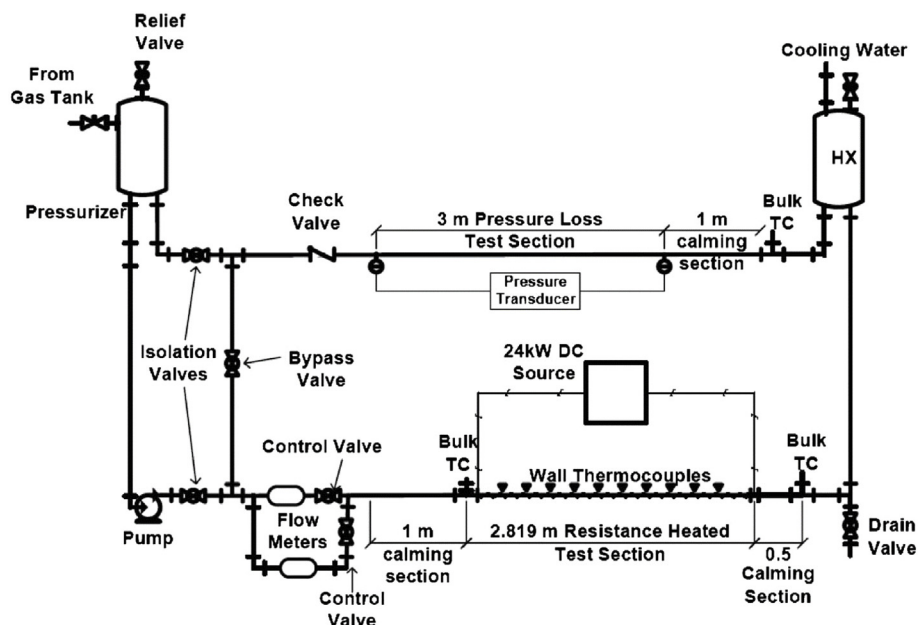

Fig. 2. Schematic of the turbulent flow convective heat transfer loop at MIT [12].

nanofluid was stored in a tank with an immersed heater (Watlow L14JX8B, 6 kW), and was driven to the loop by using a centrifugal pump (Espa XVM803F15T, 3 kW). A pre-heater (Watlow CBLC737C00S-20, 18 kW) was used to set the inlet temperature of the working fluid at constant temperature of 60 °C. Finally, the flow was directed through a set of fans in order to cool the nanofluid before coming back to the tank.

Inlet and outlet fluid temperatures were measured employing immersed thermocouples Pt100 (class B, $\pm$ 0.05 K) with a 30 mm sensing length placed across the pipe diameter. Outer wall temperatures were taken at 10 equidistant locations by using surface thermocouples Pt1000 (class B, $\pm$ 0.1 K) that were inserted 2 mm in the tube wall in order to avoid direct heating from the band heaters.

Flow rate was adjusted employing a globe valve right after the tank. An electromagnetic flow-meter (Badger Meter Magnetoflow M1000) was used to measure the flow rate. Finally, the pressure drop in the test section was also measured by using a differential pressure transducer (Inversys IDP10).

4.1.2. Preparation and characterization of nanofluid

4.1.2.1. Laminar at MIT. Nanofluids tested at MIT under laminar flow conditions were alumina Al_2O_3-water, zirconia ZrO_2-water and magnetite Fe_3O_4-water. The alumina and zirconia nanofluids were purchased from Nyacol Nano Technologies Inc. at 6 vol % and 2.6 vol % respectively [10], while the magnetite nanofluid was prepared through chemical precipitation (one step method) [11].

In the case of alumina and zirconia, the nanofluids have a vendor-specified particle size of about 50 nm. These nanofluids were used as-received except for dilution using DI-water. After dilution, full characterization of alumina and zirconia nanofluids, such as particle sizing and dispersion stability, was carried out to ensure that the stability of the nanofluid was not affected by dilution [12]. Characterization was done to assure the specifications of the colloids are as stated by the manufacturer. Detailed information on characterization of these nanofluids can be found in Williams [35]. In the case of dilution, changes of the particle size after dilution were measured to be less than 15 nm which is within the measurement uncertainty ($\pm$ 20 nm) of dynamic light scattering (DLS). The exact loading of the diluted samples before and after the flow experiments was measured with inductively coupled plasma spectroscopy (ICP). The relative difference in nanofluid concentrations before and after experiments was within 2%, which indicated no settling in the loop.

In the case of magnetite nanofluid, polymer coated magnetite nanoparticles dispersed in DI-water were synthesized through one step chemical precipitation. The detailed procedure of the magnetite nanofluid preparation is presented in Azizian et al. [11]. The composition of the magnetite nanoparticles was verified to be Fe_3O_4 using X-ray diffraction (XRD) method. The exact loading of the magnetite nanoparticles was measured with a thermogravimetric analyser (TGA). The TGA results confirmed that the weight concentration of the magnetite nanoparticles in water was 4.3% (equivalent to 0.86 vol %). DLS and transmission electron microscopy (TEM) were used to measure the particle size. Average particle size of the magnetite particles was found to be 60 nm with a very small fraction of the particles (less than 0.065 wt. %) having an average size of 150 nm.

The key parameters for assessing the heat transfer merits of nanofluids are their thermophysical properties. The density and specific heat can be readily calculated by mixture rules as mentioned in Sec. 2.

The temperature- and loading-dependent thermal conductivities for the alumina and zirconia nanofluids tested in this study were measured with a short transient hot wire apparatus, which was validated with various fluids at different temperatures and found to have $\pm$ 2% accuracy. The detailed explanation of the hot wire setup is reported elsewhere [36]. The same apparatus was used to measure the thermal conductivity of magnetite nanofluid. The dependence of thermal conductivity on loading was measured for each fluid from zero to the

associate maximum loading (in the case of magnetite nanofluid the concentration was constant at 0.86 vol %). Temperature dependence of the conductivity was measured in a temperature range of 20 °C–80 °C. The measurements show that the loading dependence of thermal conductivity is bracketed by the Maxwell-Garnet model, while the temperature dependence is the same as that of water.

Viscosity was also measured by a capillary viscometer (Cannon-Fenske Opaque) submerged in a temperature-controlled bath. The viscometer was benchmarked with water at various temperatures and its accuracy was found to be within 0.5%. Similar to the thermal conductivity measurements, temperature dependence of the kinematic viscosity was measured in a temperature range of 20–80 °C.

The curve fits to the experimental data are given below and used in the calculations [10,11].

Alumina-water nanofluid

$$k_{nf}(\phi, T) = k_{bf}(T)(1 + 4.5503\phi); \tag{4.1}$$

$$\mu_{nf}(\phi, T) = \mu_{bf}(T)\exp[4.91\phi/(0.2092 - \phi)]. \tag{4.2}$$

Zirconia-water nanofluid

$$k_{nf}(\phi, T) = k_{bf}(T)(1 + 2.4505\phi - 29.867\phi^2); \tag{4.3}$$

$$\mu_{nf}(\phi, T) = \mu_{bf}(T)(1 + 46.801\phi + 550.82\phi^2). \tag{4.4}$$

Magnetite nanofluid

$$k_{nf}(0.0086, \ T) = k_{bf}(T); \tag{4.5}$$

$$\mu_{nf}(0.0086, \ T) = \mu_{bf}(T) \tag{4.6}$$

The applicable temperature range of these equations is 20 °C < T < 80 °C with volumetric loading up to 6% for alumina and up to 3% for zirconia. Magnetite nanofluid data was measured at the constant volume concentration of 0.86 vol %.

4.1.2.2. Turbulent pipe flow at MIT. The nanofluids tested under the turbulent flow condition were colloidal alumina at 6 vol % and zirconia at 3 vol % purchased from Naycol Nano Technologies Inc. No magnetite nanofluid was tested under turbulent flow condition. Similar to the laminar flow experiments these nanofluids were used as-received except for dilution using DI-water. Similarly, full characterization of alumina and zirconia nanofluids, such as particle sizing and dispersion stability, was carried out to ensure that the specifications of the colloids were as stated by the manufacturer. The DLS results showed that the average particle size for the alumina and zirconia is about 46 nm and 60 nm respectively. These results are consistent with the average particle size of 50 nm reported by the vendor ($\pm$ 20 nm uncertainty of DLS) [12]. The temperature- and loading-dependent thermal conductivities were measured with short transient hot wire apparatus ($\pm$ 2% accuracy). Viscosity was also measured by means of a capillary viscometer submerged in a temperature-controlled bath ($\pm$ 0.5%). The experimental results for thermal conductivity and viscosity of alumina nanofluid seem to follow eqs. (4.1) and (4.2). However, as the vendor adopted a new synthesis method for zirconia nanofluid, its thermal conductivity and viscosity were re-measured for this study. It was shown that the experimental data for thermal conductivity followed eq. (4.3) with a good accuracy. However, eq. (4.7) was used for the viscosity of the zirconia nanofluid under the turbulent flow condition.

$$\mu_{nf}(\phi, T) = \mu_{bf}(T)\exp\left[\frac{11.19\phi}{(0.1960 - \phi)}\right]. \tag{4.7}$$

The applicable temperature range of these equations is 20 °C < T < 80 °C with volumetric loading up to 6% for alumina and up to 3% for zirconia.

As a standard procedure all nanofluids employed were tested for their stability at ambient temperature as well as elevated temperatures similar to their test condition. No sign of sedimentation was observed

for our nanofluids over a period of time of two weeks.

4.1.2.3. Turbulent pipe flow at UJI.
Three types of water-based nanofluids using different nanoparticles and production routes were used in the experiments at UJI [24].

The SiO_2 nanofluid was produced by the two-step method using commercial powder Aerosil 200 (Degussa) composed of amorphous hydrophilic silica nanoparticles (12 nm in diameter). The nanofluid was produced by the two-step method using an ultrasonic probe (UP400s, Hielscher Ultrasonics GmbH, Germany), and stabilized by pH value adjustment (pH = 9). Adjusting the pH value of the SiO_2 nanofluid ensures a good stability as Isoelectric point (IEP) of SiO_2 nanofluid was measured to be about 2. SiO_2 nanofluids were prepared at two different volume concentrations, 5% (Sil500) and 1% (Sil100). The mean size of agglomerates present in the resulting water suspension was found to be 201 nm for both cases as measured by dynamic light scattering system (Malvern Zetasizer Nano ZS).

The Al_2O_3 nanofluid was commercially available in suspension (AERODISP® w 925, Degussa, Germany). The nominal diameter of the nanoparticles was 11 nm. The nanofluid was stabilized by pH value adjustment (pH = 4). Commercial AERODISP® w 925 was diluted down to two concentrations, 5% (Alu500) and 1% (Alu100). An actual mean size of the agglomerates of 127 nm was identified employing DLS.

Water based nanofluid with multiwalled carbon nanotubes was commercially available as Aquacyl (Nanocyl AQ0302). MWNT's (9.5 nm diameter and 1.5 mm length) were dispersed in water with the help of Sodium Dodecylsulfate (SDS). Commercial suspensions were diluted with distilled water to achieve volume concentrations of 1% (CNTs100) and 0.125% (CNTs012).

Thermophysical properties of these nanofluids – thermal conductivity, specific heat and viscosity – were measured at several temperatures in the range of 40 °C–80 °C. Density was predicted according to the mixture rule (eq. (4.4)).

The thermal conductivity measurements were performed employing a commercial KD2 Pro conductimeter (Decagon Devices Inc.). Nanofluid's thermal conductivity was measured at three temperature conditions: 40 °C, 60 °C and 80 °C. The experimental error was obtained from the standard deviation of the measured thermal conductivity data, and it was lower than 5%.

The specific heat measurements were carried out in a Differential Scanning Calorimeter (DSC), model DSC1 (Mettler Toledo, USA). The calculation of the specific heat capacity is based on the DIN standard (DIN 51007). The DSC measures the heat flux into a sample as a function of temperature during a user-prescribed temperature map. In this study the DSC heating program consisted of three steps: Equilibrate and remain isothermal at 25 °C for 5 min, ramp from 25 °C to 95 °C at heating rate of 10 ºC/min and remain isothermal at 95 °C for 5 min. The experimental error provided by this technique is calculated to be below 6.5%.

The viscosities of the nanofluids were also measured implementing a Haake RheoStress 1 rotational rheometer (Thermo Scientific). The configuration with two concentric cylinders was used. Before each test, a pre-treatment, in which the samples were submitted to a constant shear stress, was applied to the nanofluids for 30 s to ensure similar reference conditions for all the measurements.

Finally, the stability of the nanofluids was evaluated by measuring the amount of light backscattered by each specific nanofluid from an incident laser beam during 48 h (Turbiscan Lab Expert, Formulaction SA, France). Details are given in Mondragón et al. [68].

4.1.3. Experimental procedure and error analysis
4.1.3.1. Laminar pipe flow at MIT.
The local $Nu(x)$ number is calculated based on the local thermophysical properties and local HTC, $h(x)$, as:

$$Nu(x) = \frac{h(x)d_i}{k}; \quad h(x) = \frac{q''}{T_{wi}(x) - T_b(x)} \tag{4.8}$$

where q'' is the heat flux based on the thermal power and geometry, and $T_{wi}(x)$ is the inner wall temperature. Thermal conductivity k is predicted at the mean value of inlet and outlet temperature. The latter one is calculated employing the analytical solution of the steady one-dimensional heat conduction equation in cylindrical coordinates for constant heat flux. $T_b(x)$ denotes the bulk fluid temperature at the position x and d_i is the inner pipe diameter and k is the thermal conductivity of the working fluid.

The uncertainty associated with the reported value of the Nu number was determined considering the uncertainties associated with the measurements of the individual variables in the definition of the Nu number. It was assumed that all the measured variables are uncorrelated [11].

4.1.3.2. Turbulent pipe flow at MIT.
In a way similar to the laminar flow condition, under fully developed turbulent flow condition the local Nu number and local heat transfer coefficient can be calculated based on eq. (4.8).

4.1.3.3. Turbulent pipe flow at UJI.
All the measurements were carried out at constant inlet temperature of 60 °C. The working fluid mass flux was adjusted between 100 ml/s and 2,000 ml/s to provide different Reynolds numbers. Local heat transfer coefficient and Nusselt number are calculated by using equation (4.2a-d), which still apply in this case. In order to ensure that the heat transfer measurements were taken under steady state condition, minimum time frame of 90 s as well as temperature variation of less ± 0.1 °C were reached before any measurements.

Regarding the calculation of the friction factor, measured pressure drop data was used to calculate the friction factor eq. (4.9) as

$$f = \frac{\pi^2}{8} \frac{d_i^5}{\rho L} \frac{\Delta P}{Q^2} \tag{4.9}$$

where ΔP is the pressure drop across the test section, L the distance between inlet and outlet and Q the flow rate.

The propagation of errors lead to uncertainties of 15% for the Pr number and less than 5% for the Re number. The uncertainty for the Nu number strongly depends on the Re number, being around 5% for $Re < 10,000$ and 25% for $Re > 100,000$. The errors are significantly higher at higher Re. This is due to the fact that the temperature difference between inlet and outlet of the test section was relatively small (1–3 K) at higher values of the Reynolds numbers. As the temperature difference decreases, the measurements at higher Re are affected by a higher uncertainty than those with moderate Reynolds numbers. Any attempt of reducing the uncertainty by increasing heat flux (and therefore increase the temperature change) is immediately dismissed by the activation of wall nucleation. No estimation of error is available for the friction factor as no uncertainty was obtained for the wall roughness.

4.1.4. Nusselt number correlation of reference fluid
4.1.4.1. Laminar at MIT.
The theoretical local Nusselt number can be estimated by the well-known Shah's correlation (eq. (4.10)), which is a curve fit to the complex analytical solution of the local Nusselt number for laminar flow under the constant heat flux boundary condition [37].

$$Nu_x = \begin{cases} 1.302\left(\frac{z^+}{2}\right)^{-1/3} - 0.5 \, ; & z^+ \leq 0.003; \\ 4.364 + 0.263\left(\frac{z^+}{2}\right)^{-0.506} e^{-41(z^+/2)} \, ; & z^+ > 0.003; \end{cases}$$

$$z^+ = \frac{2(z/D_i)}{RePr}; \quad Re = \frac{\rho V D_i}{\mu}; \quad Pr = \frac{c\mu}{k} \tag{4.10}$$

where z^+ is the dimensionless streamwise coordinate.

To validate the proper functionality of the experimental setup, tests were performed by reference fluid of DI-water. Initial tests with deionized water confirmed that the local Nu numbers were as predicted for

laminar flow in a round tube with constant heat flux as shown in Fig. 4 a. The solid line represents the theoretical predictions of Shah's correlation (eq. (4.10)) and the symbols represent the local Nu number calculated using the experimental data. It is clear that the measurements are within $\pm$ 10% of prediction. This result confirms the proper functionality of the flow loop.

4.1.4.2. Turbulent pipe flow at MIT. The theoretical local Nusselt number for fully developed turbulent flow condition can be estimated by the Dittus-Boelter correlation ($Re > 10,000$ and $0.7 < Pr < 120$) [37].

$$Nu_x = 0.023Re^{0.8}Pr^{0.4} \;;\; h_x = 0.023Re^{0.8}\frac{c^{0.3}k^{0.7}\mu^{0.3}}{D_i} ;$$
$$h_x = 0.023\frac{c^{0.3}k^{0.7}\rho^{0.8}V^{0.8}}{D_i^{0.2}\mu^{0.2}} . \tag{4.11}$$

The benchmark experiment was performed by reference fluid of DI-water. The results of DI-water at various Re numbers was within $\pm$ 10% of eq. (4.11) (Fig. 5 a). For ease of comprehension of the data, the tube average Nusselt number will be used. It is found that this reduces clutter and shows the desired results more clearly without loss of information [35].

4.1.4.3. Turbulent pipe flow at UJI. The heat transfer characteristics of the base fluid were measured and compared with prediction of the Gnielinski correlation. The thermophysical properties of the base fluid were obtained from standard correlations for distilled water. Figure 6 shows that the experimental values for water showed good agreement with the Gnielinski correlation for most of the experimental conditions, with deviations over $\pm$ 15% range only at low value of Re numbers.

4.1.5. Experimental results of nanofluid heat transfer

To answer some of the ambiguities about nanofluid forced convection we compared the experimental data of our nanofluids with the traditional correlations (Shah's and Dittus-Boelter) given the right

thermophysical properties of the nanofluid (i.e. measured temperature and loading dependent properties) used. If the theory successfully predicts the experimental data, this shows that the enhancement observed in HTC is the result of the change in the thermo-physical properties only and can be predicted. However, significant deviation of the experimental data from theory can signal the presence of some nanoparticle specific heat transfer mechanisms that make nanofluids behave in a fundamentally different way from homogeneous fluids. Thus, to assess the merits of the nanofluids, in this section the nanofluid experimental data (both laminar and turbulent) are compared with theory.

4.1.5.1. Laminar at MIT. The convective HTC data of nanofluids under laminar flow condition, conducted at MIT, are the ones collected by Rea et al. [10] (alumina and zirconia) and Azizian et al. [11] (magnetite).

The experimental results for the nanofluids are compared against the theory (eq. (4.10)) based on the dimensionless numbers Nu and z^+. The temperature and loading dependent properties of the fluid as described in eqs. (4.1)–(4.6) are used to derive these numbers. The results for water, alumina and zirconia at different volumetric loadings of 6 vol % and 1.32 vol % are shown in Fig. 4 a, Fig. 4 b and Fig. 4 c respectively. These two volume concentrations are representative of the general behaviour; for more data please refer to the original work of Rea et al. [10]. It can be seen that the local Nu numbers are in good agreement with the prediction of eq. (4.10), if the appropriate mixture properties are utilized. Similar behaviour was observed for the magnetite-water nanofluid [11].

By examining eq. (4.10), it is clear that under the fully developed laminar flow condition ($z^+ > 0.10$), the Nusselt number approaches a constant value and therefore the HTC is proportional to thermal conductivity while no other thermophysical property matters. Under these conditions, the estimated heat transfer enhancements for 6 vol % alumina and 1.32 vol % zirconia were 27% and 3% respectively, which is the exact enhancement observed in thermal conductivity of those nanofluids.
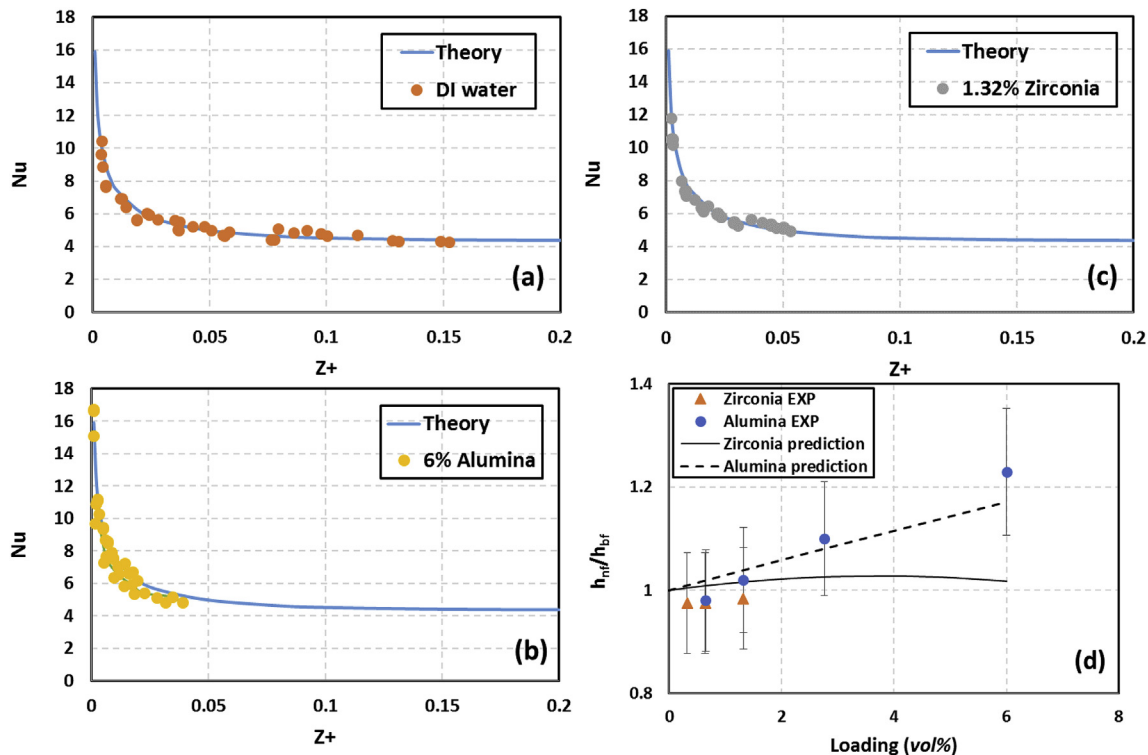

Fig. 4. Measured Nusselt numbers versus z^+ for **a**: deionized water, **b**: 6.00 vol % alumina nanofluid, **c**: 1.32 vol % zirconia nanofluid, and **d**: Heat transfer coefficient ratios of alumina and zirconia nanofluids to that of water in the entrance region.
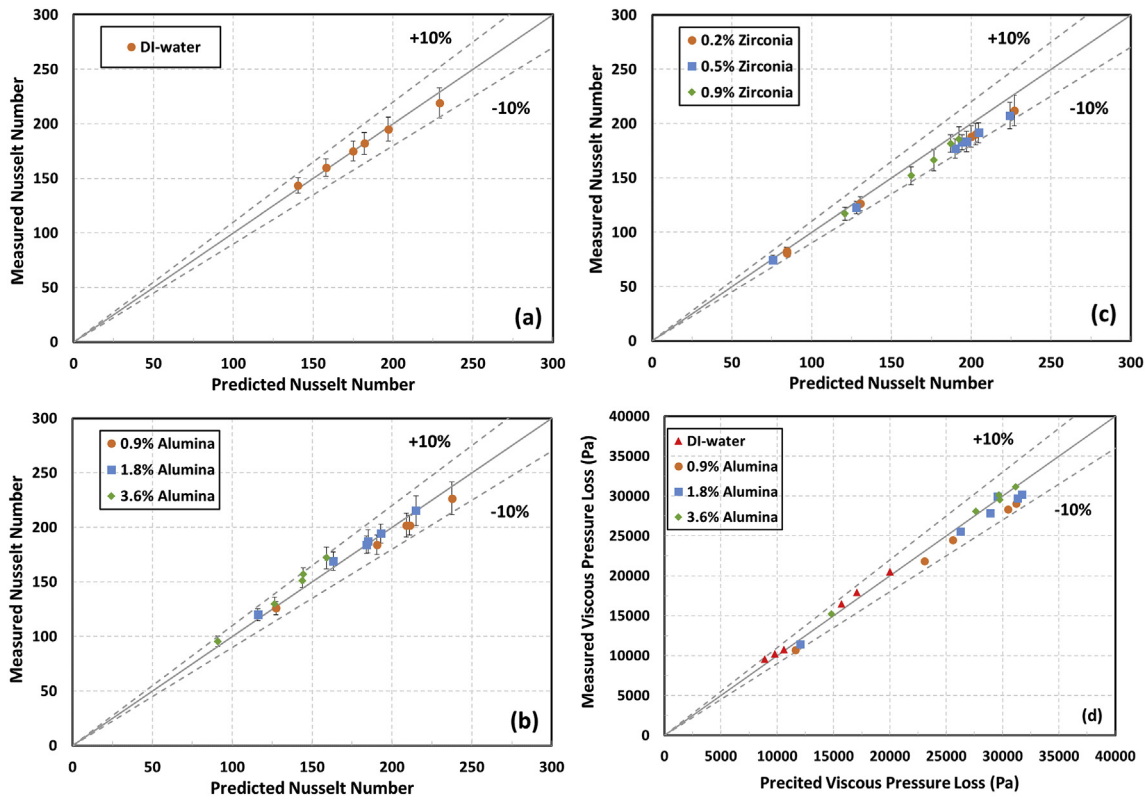
Fig. 5. Measured Nusselt numbers versus predicted Nusselt numbers for **a**: deionized water, **b**: alumina nanofluids. **c**: zirconia nanofluids, and **d**: Measured isothermal viscous pressure drop versus predicted isothermal viscous pressure drop for deionized water, alumina and zirconia nanofluids.

However, in the entrance region ($z^+ < 0.08$), using eq. (4.10), the HTC depends on thermal conductivity and also specific heat and density. From eq. (4.10) it is estimated that the heat transfer enhancements for 6 vol % alumina nanofluid and 1.32 vol % zirconia nanofluid in the entrance region are 17% and 2%, respectively. Comparison with the experimental data shows that there appears to be no abnormal heat transfer enhancement in the entrance region beyond what is predicted based on the mixture thermophysical properties (Fig. 4 d). In Fig. 4 d each experimental data point represents the average of the HTC ratios of nanofluid to water for axial locations corresponding to $z^+ < 0.01$ (where most of the *Nu* variation occurs) at various experiment conditions. The error bars represent ± 10% error as indicated previously.

In combination with the heat transfer measurements, the viscous pressure loss was also measured in the isothermal section of the flow loop for water and different nanofluids. The experimental results were compared with the pressure loss predictions for fully developed laminar flow in a circular pipe (Darcy-Weisbach equation).

$$\Delta P = f\frac{L}{D}\frac{\rho V^2}{2}; \quad f = \frac{64}{Re}. \tag{4.12}$$

The viscous pressure drops of water, alumina, zirconia and magnetite nanofluids at various concentrations were within ± 20% of the predictions [10,11]. By evaluating eq. (4.12), it can be seen that for a given flow velocity and flow geometry the pressure loss is proportional to viscosity only, which can be an issue for practical implementation of nanofluids as they tend to have very high viscosity.

4.1.5.2. Turbulent at MIT. Fully developed convective HTC of alumina and zirconia nanofluids was considered under various flow rates (9000 < *Re* < 63,000). Comparison between the measured tube average *Nu* number and calculated *Nu* number for alumina and zirconia nanofluids at different concentrations is shown in Fig. 5 b and Fig. 5 c respectively. It is clear that the measured experimental data are within ± 10% of the theory.

Equation (4.11) suggests that for a given Reynolds number, nanofluids tend to have a higher turbulent HTC than their base fluids because of their higher viscosity and thermal conductivity, in spite of a somewhat lower specific heat. On the other hand, for fixed velocity, the turbulent HTC can be enhanced or decreased, depending on the relative magnitude of the viscosity, thermal conductivity and density increase. These trends are expected and can be captured if accurate values of the thermophysical properties are available for the nanofluids of interest.

Any deviation of the data from eq. (4.11) can translate as anomalous enhancement. No such behaviour was observed in any of our experimental data. Our observations clearly showed that, what translated as
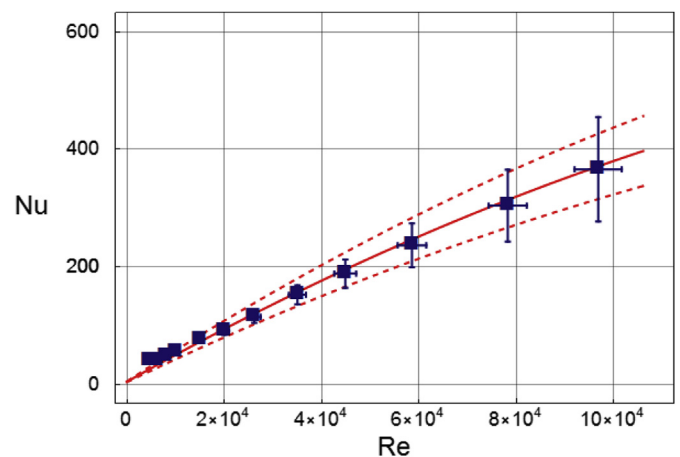

Fig. 6. Comparison between measured Nusselt numbers (symbols) versus Gnielinski correlation (red full curve) for the base fluid. Broken red curves indicate ± 15.00% of the Gnielinski correlation. (For interpretation of the references to colour in this figure legend, the reader is referred to the web version of this article.)

enhancement in nanofluids is predictable and explaining the data does not necessitate invoking any special physical phenomena occurring in nanofluids.

As the overall performance of nanofluids should be evaluated based on the trade-off between enhancement in heat transfer coefficient and undesirable increase in pumping power, the viscous pressure drop was measured under fully developed turbulent condition. The results were compared against the prediction of theory for the pressure drop (i.e. eq. (4.12)) where the friction factor can be determined either from the Blasius relation ($f = 0.316Re^{-0.25}$ for $Re < 30,000$) or the McAdams relation ($f = 0.184\,Re^{-0.2}$ for $Re > 30,000$). Fig. 5d shows the experimental pressure drop data in comparison to the predicted viscous pressure drop of eq. (4.12). It can be seen that the isothermal viscous pressure drops of water, alumina and zirconia nanofluids at various concentrations were within ± 10% of the predictions.

4.1.5.3. Turbulent pipe flow at UJI. Fig. 7 compares the experimental values of the Nusselt number, Nu_{exp}, against the ones provided by the Gnielinski correlation, $Nu_{Gnielinski}$. This comparison is shown in terms of the Nusselt number ratio, Nu_{ratio}, that is defined as

$$Nu_{ratio} = \frac{Nu_{exp}}{Nu_{Gnielinski}}. \tag{4.13}$$

The theoretical values for the turbulent friction factor were also calculated by using the Colebrook–White correlation. The wall roughness of the test section was estimated by fitting the experimental data for the DI-water to the prediction of the Colebrook–White correlation. Figure 8 shows the comparison between the measured friction factor
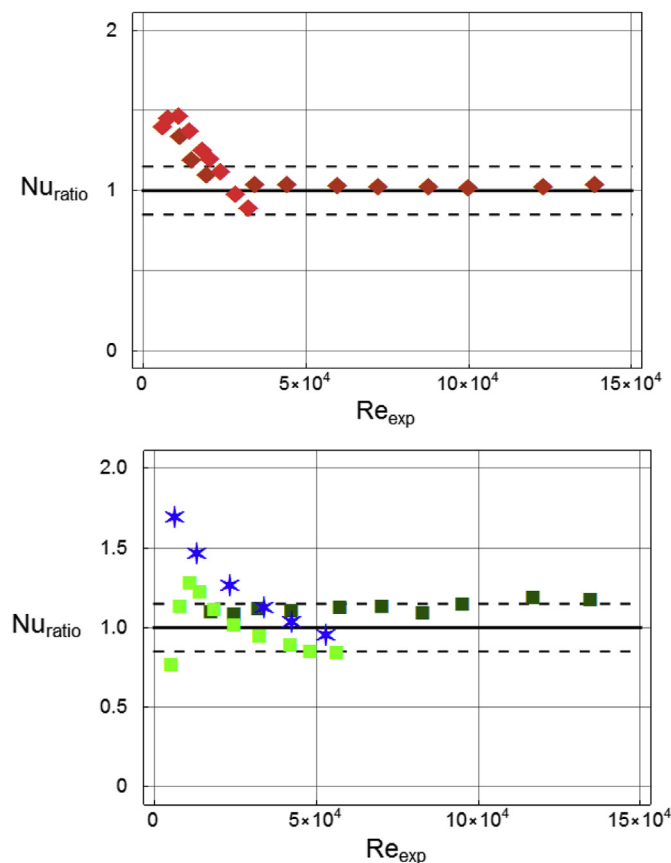
Fig. 7. Comparison between measured Nusselt numbers and Gnielinski's correlation for turbulent pipe flow. Upper plot shows Si100 (dark red) and Si500 (red). Lower plot shows Al100 (dark green), Al500 (green) and CNT (blue stars). (For interpretation of the references to colour in this figure legend, the reader is referred to the web version of this article.)
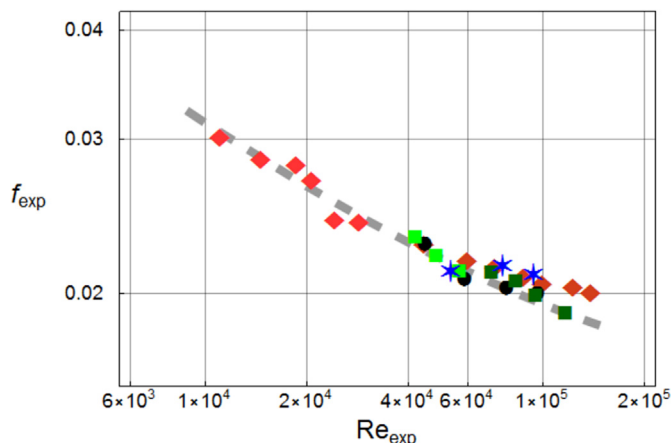
Fig. 8. Comparison between measured friction factor and Colebrook-White correlation for water and the nanofluids. Symbols as in Fig. 7.

and the predictions given by the Colebrook–White equation under turbulent flow conditions. No error bars appear in this plot as the main source of error, i.e. the wall roughness, was not directly measured. Instead, its value was calculated so that the water pressure drop matches the prediction of the correlation.

Finally, Fig. 9 compares the heat transfer coefficients for the nanofluids under a constant pumping power basis. Note that the heat transfer coefficient for all nanofluids is reduced with respect to that of water at any given pumping pressure. In addition, the comparison worsens with increasing nanoparticle concentration.

As expected the experimental data obtained at UJI show very good agreement with standard correlations (see Table 3) for the heat transfer coefficient under turbulent flow conditions, especially for values of $Nu > 150$ for which the flow can be considered fully turbulent. As can be seen in Table 3, if all nanofluids are considered, the best results are obtained by the Gnielinski correlation followed by the Sieder-Tate and Dittus-Boelter correlations.

4.2. Flow in straight pipe with circular cross section and inserted twisted tape (ILK, Germany)

There have been numerous attempts to increase heat transfer in annular pipes employing inserts (Bergles [38]). The most prominent one is the so-called twisted tape. The general idea is to place a warped band of limited thickness inside the tube. The tape is twisted in such a way that two separated chambers oriented in the streamwise direction
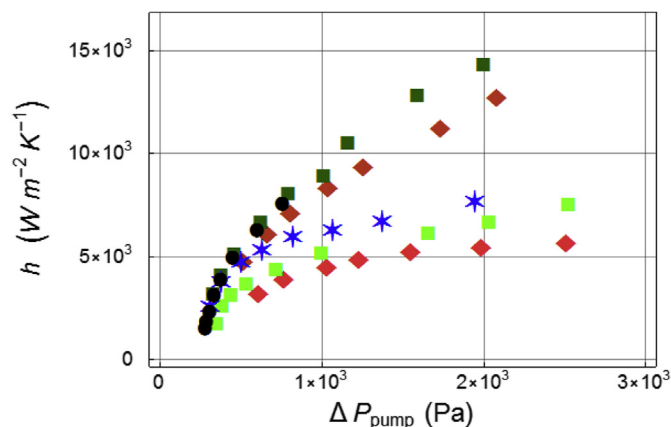

Fig. 9. Heat transfer performance of the nanofluids studied and the reference fluid (water) on a constant pumping power basis. Symbols as in Fig. 7. Black dots indicate pure water.

Table 3

Correlation coefficients for different heat transfer correlations turbulent pipe flow at UJI.

Nanofluid	Gnielinski	Dittus-Boelter	Sieder-Tate
Sil500	0.81	0.70	0.89
Sil100	0.98	0.69	0.70
Alu500	0.88	0.98	0.94
Alu100	0.91	0.45	0.50
CNTs012	0.88	0.67	0.87

are created. The flow is forced to spin so that a radial force is generated. This force in turn causes a pair of counter-rotating vortices in each of the two chambers. These secondary flows mix the fluid inside the chambers and therewith break the more or less stable radial temperature distributions which otherwise would develop.

Due to the high practical relevance, it is worth investigating if the heat transfer obtained with a pipe with inserted twisted tape can be further enhanced when a nanofluid is employed as heat carrier.

4.2.1. Description of test rig

Experiments on heat transfer laminar flow in a pipe with twisted tape were carried out at ILK-Dresden (Buschmann, [39]). The employed test rig (Fig. 10) consisted of a circular copper pipe with an inner diameter of 7.88 mm (nominal 8.00 mm) and an outer diameter of 14.00 mm. The heated length of the pipe was 1500.00 mm. An unheated entrance pipe of 400.00 mm length ensured that a fully developed laminar profile (Hagen-Poiseuille profile) entered the heated section. The inserted twisted tape was manufactured from a 1.00 mm thick copper band. The pitch to diameter ratio was about six. For Reynolds number prediction, the tape thickness was considered.

An electric heater (High Performance Tubular Heater, Türk + Hillinger Elektrowärme, Germany), which provided a constant heat flux, jacketed the heated pipe section. Two copper half-shell parts pressed the heater together to avoid its disconnection from the pipe during operation. Unheated and heated pipe sections were insulated with a 20.00 mm insulation shell made of ARMAFLEX (Armacell, Germany). The working fluid, either DI-water or nanofluid, was driven through the loop by an oscillating piston pump (AFT GmbH and Co. KG, Germany). After leaving the heated pipe section, the working fluid was cooled employing a stainless steel heat exchanger. All tubes connecting parts of the test rig were made of Teflon® coated hoses (Rotilabor®-PTFE

hose, ROTH, Germany) to avoid chemical interaction. Because the nanofluid used was photochemically reactive, all tubes were covered with opaque aluminium foil. Directly downstream to the outlet of the heated section an unheated outlet section was positioned to disconnect the test section from following tube bends etc. Following this outlet section a buffer bottle made of glass was mounted which was also covered with aluminium foil (Fig. 10). Short-time opening of the foil allowed inspection of the working fluid during operation. No noticeable problems (changes of colour, contamination etc.) were observed during the experiments.

Ten k-type thermocouples (Newport Omega, GB, uncertainty 0.75%) were positioned on the upper centre line of the pipe (x = 40, 65, 112, 162, 302, 512, 762, 1012, 1262 and 1462 mm). The thermocouples were fixed employing thermally conductive paste in 1.00 mm deep holes drilled into the mantle of the pipe.

Fluid inlet and outlet temperatures were measured employing Pt100 (class A, maximum uncertainty 0.50%). Volume flux was quantified with the aid of a magnetic inductive flow metre (OPTIFLUX 5300 W, KROHNE Messtechnik GmbH and Co. KG, Germany, uncertainty 0.10%).

4.2.2. Preparation and characterization of nanofluid

Commercial water-based titanium dioxide suspensions of 5 vol % and 10 vol % (AERODISP®W740X, EVONIK Degussa GmbH, Germany) were utilized as nanofluids. Both concentrations were dilutions of the original suspension with 12.70 vol % (pH 6.3 at 25.00 °C [40]). According to the producer, nanoparticle size should be between 30 nm and 80 nm. Particle size analysis (Zetasizer Nano ZS, Malvern Instruments GmbH, Germany, reproducibility less than ± 5.00%) indicated a size of 85 nm. Production route of the original suspension was two-step, but not further specified by the producer. According to the product information of AERODISP®W740X [65] the liquid should be used within 12 months after fabrication. This was followed because experiments were carried out within two to four months after production. Optical observations with the naked eye showed that the original suspension was stable against sedimentation for at least six months at room temperature.

Thermal conductivity (Fig. 11) was determined between 20 °C and 60 °C (increment 10.00 K) employing a ring gap apparatus [42,43]. Measurement error was less than ± 1.00%. Due to the high particle load, a significant average increase of thermal conductivity of 12.00% for a concentration of 5.00 vol % and of 22.00% for a concentration of
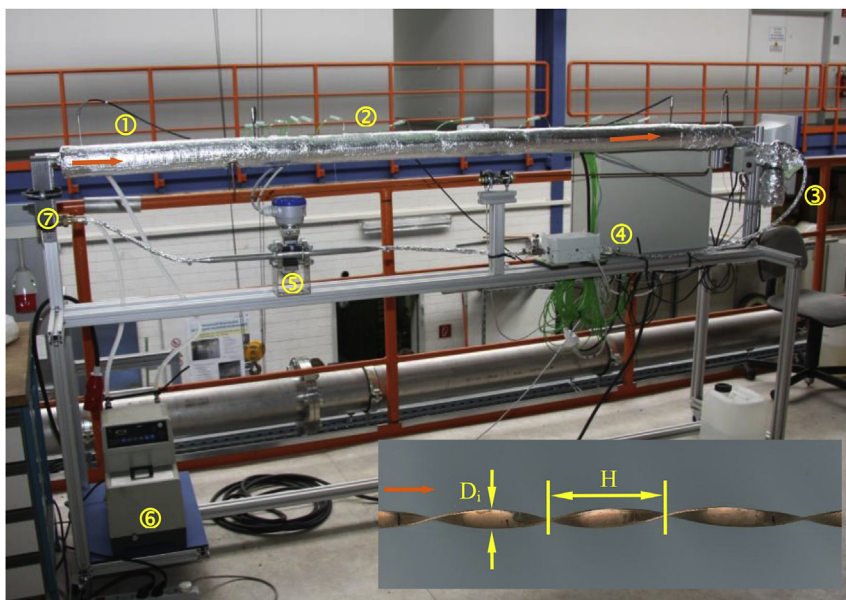

Fig. 10. Test facility and twisted tape (insert). The main components are ① entrance length, ② test section with thermocouples, ③ buffer bottle made of glass, ④ pump, ⑤ flow metre, ⑥ thermostat, ⑦ heat exchanger. The lower photo provides details of one of the thermocouples inserted into the pipe wall. Orange arrows indicate flow direction. (For interpretation of the references to colour in this figure legend, the reader is referred to the web version of this article.)
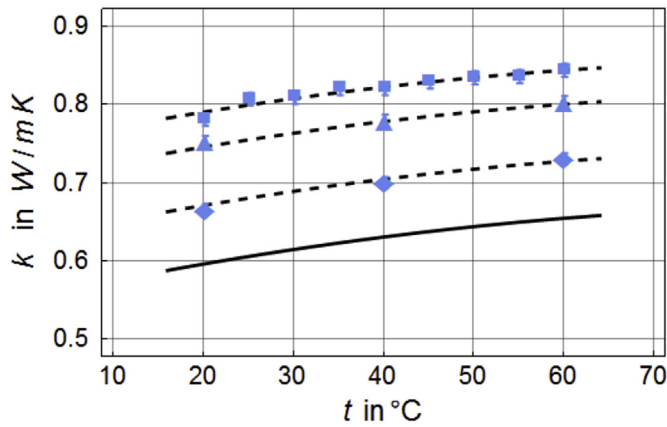
Fig. 11. Experimentally determined thermal conductivity of titania nanofluids for experiments in pipe flow with twisted tape. Bold curve indicates thermal conductivity of DI-water according to NIST-database [41]. Broken curves indicate fit of experimental data.

10.00 vol % was found.

Viscosity was determined for dilutions of 3 vol %, 5.00 vol %, 7.00 vol %, and 10.00 vol % (Fig. 12) employing a rotational viscometer (Viscotester VT 550, HAAKE, Germany, uncertainty ± 3.00%). The results were in excellent agreement with the theory proposed by Chevalier et al. [44]. Independent measurements employing Rheometers MCR 301 (Fa. Anton Paar, Graz, Austria, torque accuracy max. 0.50%) indicated a weak shear thinning behaviour (flow behaviour index of 0.952, standard deviation 0.019) of the original suspension (12.70 vol %). This behaviour was not confirmed for the 5.00 vol % suspension. Therefore, taking all viscosity results together, a non-Newtonian behaviour is unlikely for the suspensions employed for the experiments.

Thermal conductivity and viscosity data were fitted as function of concentration and temperature. Only these fits were employed for the calculation of the Reynolds and Prandtl numbers. Density was predicted according to eq. (1.4).

4.2.3. Experimental procedure and error analysis

Measurements were carried out for water and nanofluids at a constant inlet temperature of 20.00 °C. Volume flux of the working fluid was varied between 7.00 l/h and 35.00 l/h to change the Reynolds number. Based on local thermophysical properties and local heat transfer coefficient $h(x)$, the local Nusselt number $Nu(x)$
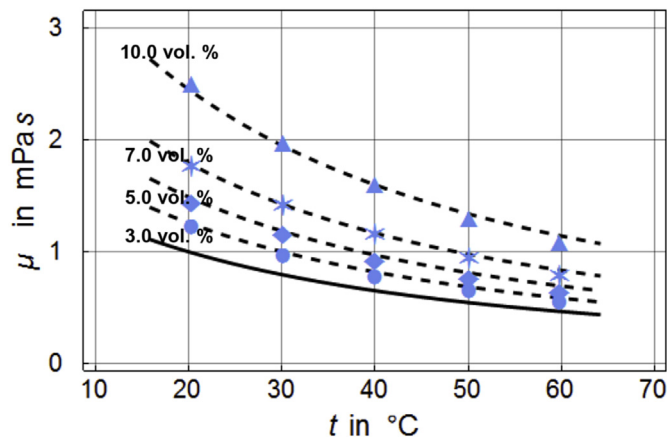
Fig. 12. Experimentally determined viscosity of titania nanofluids with different concentrations for experiments in pipe flow with twisted tape. Bold curve shows viscosity of deionized water according to the NIST database [41]. Broken curves indicate the model according to Chevalier et al. [44].

$$h(x) = \frac{q_w}{T_{wi}(x) - T_{bi}(x)}; \quad Nu(x) = \frac{h(x)\, d_i}{k} \tag{4.14}$$

is predicted. Thermal conductivity of nanofluids has been determined experimentally in a temperature range between 20 °C and 60 °C [42,43]. Bulk flow T_{bi} follows from

$$T_{bi}(x) = T_{in} + \frac{q_w\, \pi\, d_i}{\dot{m}\, c_p}\, x; \tag{4.15}$$

and the temperature at the inner pipe wall T_{wi} is calculated according to the steady one-dimensional heat conduction equation in cylindrical coordinates for constant heat flux

$$T_{wi}(x) = T_{wci}(x) - \frac{Q\, d_i\, ln(d_{tc}/d_i)}{2\, k_{co}}. \tag{4.16}$$

Here Q is the wall heat flux with the internal surface as a reference. The measured temperature at the position x_i of the thermocouple i is T_{wci}, while d_i and d_{tc} are the inner pipe diameter and the diameter at which the thermocouples are positioned. The length of the pipe is l, and k_{co} denotes the thermal conductivity of the pipe material copper.

Employing Gauss' law of propagation of uncertainty, the relative errors of 1.50% for Pr, 2.00% for Re, and, 5.00–8.00% for Nu are obtained. The amount of heat transferred is predicted with an uncertainty of about 1.10%.

4.2.4. Nusselt number correlation of reference fluid

Laminar and turbulent flow of classical fluids in pipes with inserted twisted tape have been investigated in numerous studies (Manglik and Bergles, [45–47]). Several Nusselt number correlations that depend on the Reynolds, Prandtl, Rayleigh, and Grätz numbers, pitch to diameter ratio, gap between tape and inner pipe, etc. have been published [47]. However, for the investigation presented here, none of these correlations were employed. The reason is that the goal of the study is to validate if parameters such as the concentration characterising a nanofluid must also be part of the Nusselt number correlation sought after. Therefore, results obtained with the reference fluid DI-water and nanofluid flows were compiled and fitted employing the Levenberg-Marquardt algorithm implemented in MATHEMATICA 10.0. The quality of these fits was then verified and employed to judge whether or not the nanofluid parameters improve the correlation [39].

4.2.5. Experimental results of heat transfer and pressure loss

Experiments were carried out with the inlet Reynolds numbers ranging roughly between 400 and 1,200. For an inlet temperature of 20.00 °C, the inlet Prandtl number of DI-water is 6.99. Significantly higher inlet Prandtl numbers – 11.57 for 5.00 vol % and 13.87 for 10.00 vol % – have to be considered for the nanofluids. Data were processed based on the idea that a Nusselt number correlation should in general have a form of

$$\overline{Nu} = f\,(GEO,\, Re^n,\, Pr^m). \tag{4.17}$$

Here $\overline{Nu}$ denotes the Nusselt number averaged over the entire heated pipe. Because the pipe and the insert are not changed during experiments, the correlation is written without considering geometrical parameters. Ordering the data alone according to the Reynolds number would reduce the analysis to the influence of flow dynamics. Considering the Prandtl number includes the effects of thermophysical properties of the working fluids. The powers n and m weight these influences and have to be determined from fitting the data.

A perfect collapse of all data (Fig. 13) – DI-water and nanofluids – is achieved with

$$\overline{Nu(Re_i,\, Pr_i)} = 0.255\,(Re_i Pr_i^{0.391} - 13.717)^{0.526}$$
$$700 \leq Re_i Pr_i^{0.391} \leq 2{,}900\,. \tag{4.18}$$

Nanofluid data with a concentration of 5.00 vol % not considered in the fitting procedure (green rhombi in Fig. 13) confirm eq. (4.18).
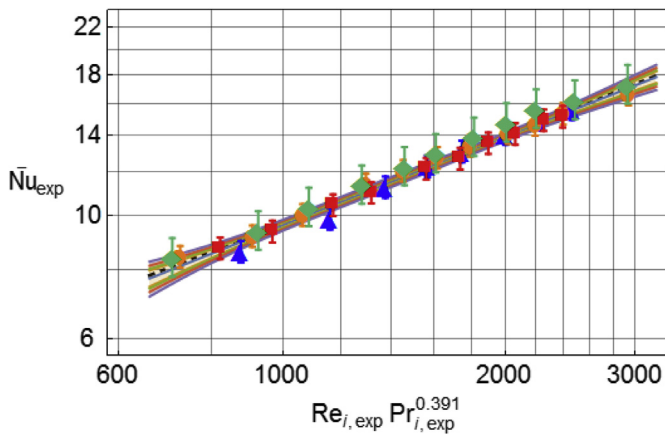
Fig. 13. Averaged experimental Nusselt number (eq. (4.18)) for experiments in pipe flow with twisted tape. Blue triangles stand for DI-water, orange dots for nanofluid with 5.00 vol %, and red squares for nanofluid with 10.00 vol %. Broken line indicates eq. (4.18) obtained from DI-water and nanofluid (orange and red) data. Green rhombi show nanofluid data (5.00 vol %) not considered in the fit for eq. (4.18). Bands show confidence levels of 90.00%, 95.00%, 99.00%, and 99.90% (from outside to inside). (For interpretation of the references to colour in this figure legend, the reader is referred to the web version of this article.)

Standard error and confidence interval of parameters appearing in eq. (4.18) are given in Table 4.

The general finding represented with eq. (4.18) and Fig. 13 is that the Nusselt number obtained for a certain value of $Re_iPr_i^{0.391}$ is independent of the nanoparticle concentration. This indicates that no parameters characterising the nanofluid are additionally needed to complete eq. (4.17) and eq. (4.18). A crosscheck confirmed that no improvement is obtained by including nanoparticle concentration as an independent parameter [39]. Moreover, if the Nusselt number is not varied by adding nanoparticles to the working fluid but the thermal conductivity of nanofluid is increased (Fig. 11), it is obvious that the heat transfer coefficient h can be only enhanced by the same amount as the increase of the thermal conductivity. Figure 14 shows the ratio of the heat transfer coefficients of nanofluid and DI-water experiments and indeed the enhancement of the average heat transfer coefficient is within the experimental error equal to the increase of the average thermal conductivity.

Results for pressure loss are compiled in Fig. 15. Experiments carried out in the empty pipe show reasonably good agreement with the classical relation for the laminar friction factor $f = 64/Re$. Data for DI-water and nanofluid flow in the pipe with inserted twisted tape collapse on one single curve. Once again, this finding indicates that titania nanofluid flow can be described with the same correlation as the pure base fluid flow and no unusual phenomena occur.

4.3. Flow in a coil heat exchanger (Lund University, Sweden)

Helically coiled tubes and coil heat exchangers are promising devices to enhance heat transfer due to their high heat and mass transfer coefficients, compact design, narrow residence time distributions and ease of manufacture. The flow field in helically coiled tubes is affected

Table 4
Standard error and confidence interval of parameters appearing in equation (4.18).

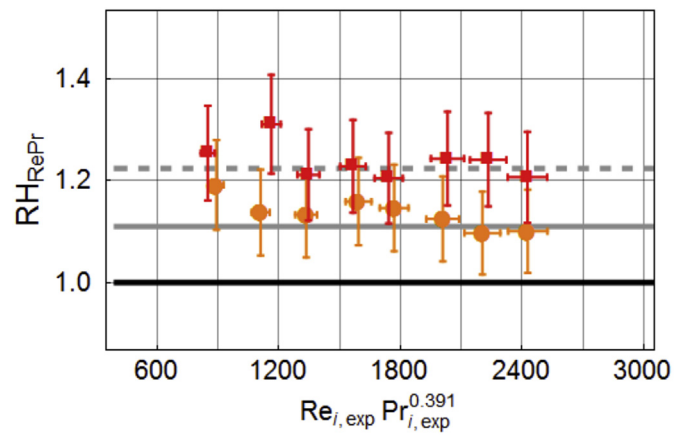| Estimate	Standard error	Confidence interval
0.255	0.122	−0.004–0.510
13.717	148.402	−318.762–291.327
0.526	0.058	0.408–0.645

Fig. 14. Ratios of heat transfer coefficient for $Re_i{}^m Pr_i{}^n$ – scaling for experiments in pipe flow with twisted tape. Symbols are as Fig. 13. Full lines indicate averaged increase of thermal conductivity for concentration of 5.00 vol % and broken line for 10.00 vol %.

by centrifugal forces, which induce a secondary flow field with a couple of vortices in the cross-section of the tube. The fluid in the central part is driven towards the outer wall by the centrifugal force, then returns to the inner wall by flowing back along the wall, as illustrated in Mori and Nakayama [48]. Compared with straight tubes, the above-mentioned secondary flow in helically coiled geometries improves heat transfer rates as it reduces the temperature gradient across the tube cross-section, producing an additional convective heat transfer mechanism perpendicular to the main flow. This section aims to summarize the experimental investigations carried out at Lund University [49,50] on the performance of nanofluids in a coil heat exchanger.

4.3.1. Description of test rig

A schematic illustration of the test rig is shown in Fig. 16. It consists of two loops, with the working fluid (either DI-water or nanofluid) flowing in a closed loop and water flowing in an open loop (as a coolant), respectively. The working fluid is heated in a 50-L reservoir by an imbedded electric heater of 6 kW fixed at the bottom of the reservoir. The working fluid is pumped from the reservoir, and then it passes a control valve, enters the inner helically coiled tube of the coil heat exchanger, goes into a rotameter, and returns to the reservoir. For the cold loop, the coolant (water in this case) flows through the pump from a water tank, passes a control valve, enters the rotameter for volume flow rate measurement, and then goes into the annulus counter-
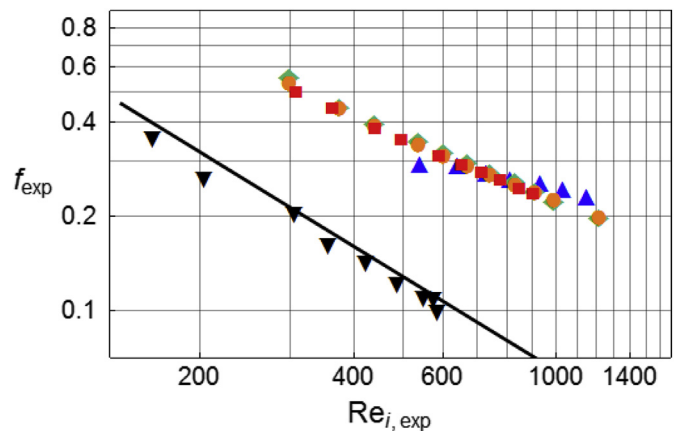

Fig. 15. Dependence of friction factor on the inlet Reynolds number for experiments in pipe flow with twisted tape. Symbols are as Fig. 13. Downward triangles show reference measurements with water for the empty pipe. Full line indicates $f_{exp} = 64/Re_{i,exp}$.
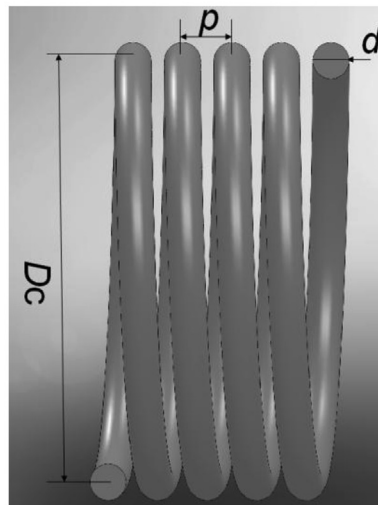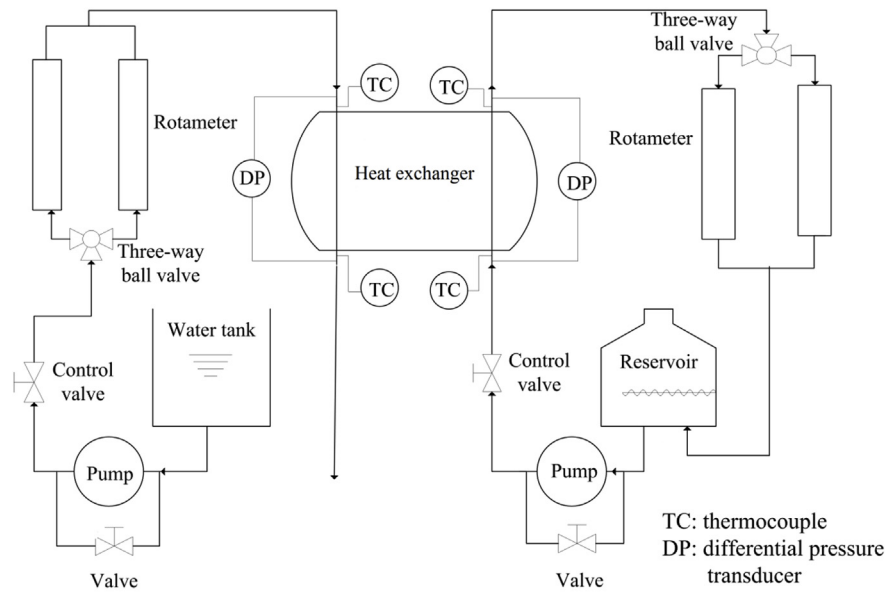
Fig. 16. Schematics of the test rig (top) and a helically coiled tube (bottom).

currently. Each loop has two rotameters of small and large ranges for accurate flow rate measurements. A differential pressure transducer with an accuracy of ± 0.075% of the set span was used to measure the pressure drop across the inner tube. All rotameters were calibrated for water and nanofluids of different concentrations at different temperatures by using a stopwatch and a constant volume container with a maximum uncertainty of 2.00% at the lowest flow rate. The inlet and outlet temperatures of the inner tube and the annulus were measured by four calibrated copper-constantan thermocouples with an accuracy of ± 0.1 K, respectively. All temperature measurements were recorded by a data logger.

The double-pipe helically coiled heat exchanger considered in this section was constructed by copper tubes and standard copper connections. The inner helically coiled tube, also shown in Fig. 16, has an inner diameter (d_i) of 13.28 mm. The outer surface of the inner tube was enhanced by circular fin arrays (not shown in Fig. 16) with a fin height of 3.20 mm. The ratio of the outer surface area (A_o) to the inner surface area (A_i) of the inner tube is 4.83. The outer helically coiled tube has an inner diameter of 26 mm. The approximate hydraulic

diameter of the annulus side (d_a) is 8 mm (fin arrays not considered). The number of turns (n) of the helical coils is 4.5, and each coil has a coil diameter of curvature (D_c, measured from the centre of the inner tube) of 254 mm. The pitch of the helical coil (p) is 34.5 mm. The total length of the tested helical heat exchanger is 3.591 m.

4.3.2. Preparation and characterization of nanofluid

Two types of nanofluids were prepared and characterized, i.e., γ-Al_2O_3/water nanofluids of six concentrations, and multi-walled carbon nanotube (MWCNT)/water nanofluids at three different concentrations. Untreated concentrated γ-Al_2O_3/water nanofluid with spherical alumina nanoparticles of 40-nm mean diameter (according to the producer) was purchased from a commercial company (Nanophase Technologies Corporation, US). No surfactants were added in the nanofluid. Different amounts of concentrated nanofluid were diluted in water to obtain nanofluids with low concentrations. The diluted nanofluid mixture was mechanically stirred for 0.5 h followed by ultrasonic vibration for 3 h. The pH value of the prepared alumina nanofluid is about 3–3.5, which is far away from the iso-electric point of alumina

Table 5
Thermal conductivity and viscosity enhancement values of nine nanofluids measured at a temperature of 20.00 ± 0.50 °C (flow in a coil heat exchanger).

Nanofluid	Volume concentration (weight concentration)	Thermal conductivity enhancement relative to water	Viscosity enhancement relative to water nanofluid
γ-Al$_2$O$_3$/water	0.20 vol % (0.78 wt. %)	0.96%	0.15%
	0.56 vol % (2.18 wt. %)	2.25%	0.59%
	1.02 vol % (3.89 wt. %)	3.25%	5.68%
	1.50 vol % (5.68 wt. %)	4.31%	11.11%
	1.88 vol % (7.04 wt. %)	5.16%	13.68%
	2.84 vol % (10.56 wt. %)	8.10%	20.00%
MWCNT/water	0.0111 vol % (0.02 wt. %)	0.07%	12.99%
	0.0278 vol % (0.05 wt. %)	0.20%	15.87%
	0.0555 vol % (0.10 wt. %)	0.42%	20.66%

nanofluid (~9) to maintain colloidal stability.

Sedimentation and agglomeration of nanoparticles and their dispersion stability is important to keep conditions unchanged during the experiments. At the preparation stage these aspects were taken into account. Parameters affecting the stability are, e.g., preparation methods, nanoparticle mean diameter, nanoparticle aggregation states, types of nanoparticles and base fluid [66,67] were carefully controlled. Optical observations with the naked eye showed that the nine suspensions prepared were stable against sedimentation for at least two weeks at room temperature. In the present experiments we are convinced that the nanofluids did not interact with the test rig and had not left any contaminations behind as tests with only the pure base fluids before and after the nanofluids tests showed fully consistent results.

An aqueous MWCNT suspension of 1.00% mass fraction was purchased from a commercial vendor (Nanocyl, Belgium). According to product specifications, the suspension consists of MWCNTs dispersed in de-ionized (DI) water (97.00% mass fraction) and stabilized with sodium dodecyl benzene sulfonate surfactant (SDBS, 2.00% mass fraction). The MWCNTs, produced via the catalytic carbon vapour deposition process, have an average length of 1.50 μm and an average diameter of 9.50 nm, with an average aspect ratio of 158. The surface area of the MWCNT is 250–300 m^2/g. The carbon purity of the MWCNTs is 90.00%, while the remaining 10.00% is metal oxide. Similar to alumina nanofluid, different amounts of concentrated nanofluid were diluted in water to obtain MWCNT/water nanofluids with different fractions. The diluted nanofluid mixture was mechanically stirred for 10 min followed by ultrasonic vibration for 1 h. The pH values of the prepared MWCNT/water nanofluids are in the range of 7.00–8.00.

The thermal conductivity and viscosity of the nine nanofluids were experimentally measured. A thermal constants analyser (TPS 2500S from Hot Disk AB, Sweden) using the transient plane source method (TPS) was employed to measure the thermal conductivity. Its uncertainty was estimated from the standard deviations of experimental data and departures from literature data, to be less than 3.00%. A rotational rheometer HAAKE RS6000 (Thermo Fisher Scientific Inc., US) was also used to measure the rheology behaviour of those nanofluids. The standard deviation of the dynamic viscosity data of the DI-water (the base fluid implemented in all of the experiments here) was less than 3.00%. The thermal conductivity and viscosity data of the nanofluids at 20.00 ± 0.20 °C are listed in Table 5.

4.3.3. Data reduction and error analysis

The transferred heat amount Q was averaged between the heat transferred by inner hot fluid Q_h and the heat absorbed by the annulus cold water Q_c:

$$Q = \left(\frac{Q_h + Q_c}{2} \right) = \left[\frac{c_{p,h} \dot{m}_h (T_{hi} - T_{ho}) + c_{p,c} \dot{m}_c (T_{co} - T_{ci})}{2} \right]. \qquad (4.19)$$

The maximum deviation in energy balance between the inner hot side and the annulus cold side is less than 1.00%. The logarithmic mean temperature difference (LMTD) was determined by the following equation

$$LMTD = \frac{(T_{hi} - T_{co}) - (T_{ho} - T_{ci})}{\ln\left[(T_{hi} - T_{co})/(T_{ho} - T_{ci})\right]}. \qquad (4.20)$$

Assuming no fouling resistance and ignoring the wall thermal resistance due to the thin wall, large tube length and high thermal conductivity of copper, the inner tube heat transfer coefficient h was determined by

$$h = \frac{1}{A_i \left[\frac{LMTD}{Q} - \frac{1}{h_a A_o} \right]}. \qquad (4.21)$$

The annulus thermal resistance in the above equation was also neglected because of the following reasons: (1) the annulus heat transfer coefficient h_a is relatively large due to the intensive turbulence induced by the fins on the outer surface of the inner tube; (2) $A_o/A_i = 4.83$; (3) the volumetric flow rate on the annulus side was kept relatively large during the experiments; (4) a minor change in h was noticed for a 20% change of the annulus flow rate during the experiments. Thus, eq. (4.3c) can be simplified as

$$h = \frac{Q}{A_i LMTD}; \qquad (4.22)$$

$$Nu = \frac{hd_i}{k}. \qquad (4.23)$$

Only the inner tube heat transfer coefficient was investigated and evaluated in this study. The propagated uncertainties of h, Nu and Pr are 3.50%, 4.60% and 4.20%, respectively. All properties used in the dimensionless numbers were calculated at the average bulk fluid temperature which was estimated from the inner-tube inlet and outlet temperatures.

Before and after the nanofluid tests, water experiments were conducted in the same double-pipe coil heat exchanger to make sure no nanoparticle settlement has happened during the tests with nanofluid, see Wu et al., [49]. The water experimental data points before and after the nanofluid tests present very similar thermal behaviours, indicating very small and negligible deposition of nanoparticles during the nanofluid tests.

4.3.4. Nusselt number correlation of the reference fluid

The transitional Reynolds number from laminar to turbulent flow is approximately 6,000 for coil tubes. For laminar flow in the tested coil tube, a new heat transfer correlation was proposed by Wu et al. [49] for water flowing inside helically coiled tubes:

$$Nu_b = 0.089 De_b^{0.775} Pr_b^{0.4}, \qquad (4.24)$$

where the Dean number De is a function of the Reynolds number and the ratio of the tube diameter to the coil diameter:

$$De = Re\left(\frac{d_i}{D_c} \right)^{0.5}. \qquad (4.25)$$

The coefficient of determination for the fitting correlation, R^2, is
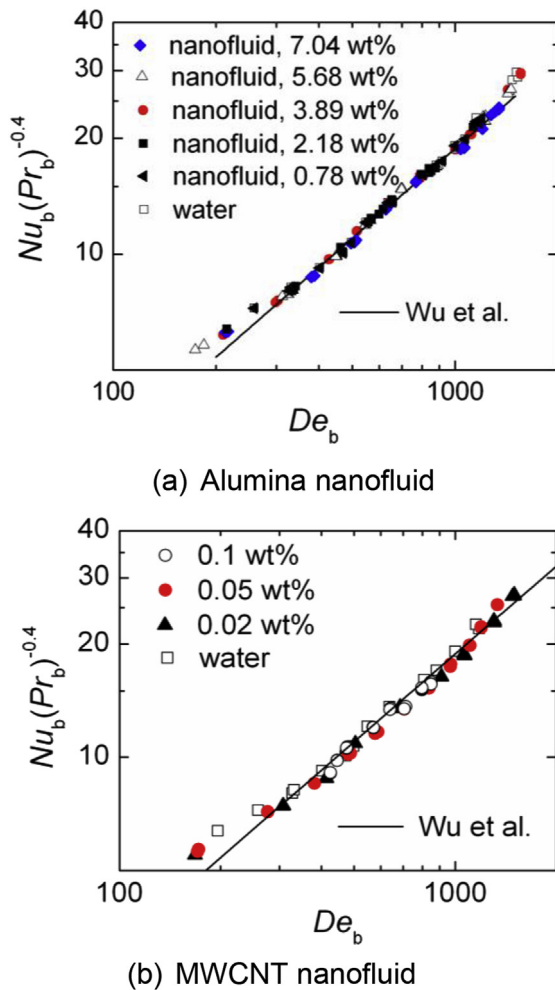
(a) Alumina nanofluid

(b) MWCNT nanofluid

Fig. 17. $Nu_b(Pr_b)^{-0.4}$ vs. De_b for laminar flow against the Wu et al. [49] correlation (data from Refs. [49,50]).

equal to 0.995, indicating that the correlation fits the data very well. The mean absolute error e_A and standard deviation σ_N of the correlation are 2.30% and 2.90%, respectively. The applicable range of the correlation is: $100 < De < 1300$ and $4.00 < Pr < 7.00$.

For turbulent flow in the inner coil tube, the Seban and McLaughlin [51] correlation can predict the thermal behaviour of water very accurately, with a mean absolute error and a standard deviation of 2.60% and 3.10%, respectively. The Seban and McLaughlin [51] correlation is given below

$$Nu_b = 0.023Re_b^{0.85}Pr_b^{0.4}(d/D_c)^{0.1}. \tag{4.26}$$

The applicable range of the Seban and McLaughlin [51] correlation is: $6{,}000 < Re < 65{,}600$, $2.90 < Pr < 5.70$.

4.3.5. Experimental heat transfer results of nanofluids

For nanofluids, the transitional Reynolds number from laminar to turbulent flow for coil tubes is approximately the same as that for water [49,50]. Figure 17 demonstrates the relationship between $Nu_b(Pr_b)^{-0.4}$ and the inner tube Dean number De_b for laminar flow. Fluid properties in the dimensionless numbers were based on the average bulk temperature. Nanofluid properties measured at the average bulk temperature were used. As shown in Fig. 17, the Nusselt number increases with the Dean number. Water, the five alumina nanofluids and the three MWCNT nanofluids present very similar heat transfer characteristics. The water and nanofluid data can be estimated accurately by the same correlation eq. (4.24). As this correlation is independent of the nanoparticle concentration (in fact the concentration is embedded in the

thermophysical properties), no additional parameters characterising the nanofluids are needed to evaluate the heat transfer performance of nanofluids.

Fig. 18 presents the relationship between $Nu_b(Pr_b)^{-0.4}$ and the inner tube Reynolds number Re_b for the turbulent flow. It is clear that $Nu_b(Pr_b)^{-0.4}$ increases with Re_b and similar to the laminar flow condition the eight nanofluids and water show very similar trends. The Seban and McLaughlin [51] correlation can predict the thermal behaviour of water and nanofluids very accurately, with a mean absolute error and a standard deviation of 2.63% and 3.25%, respectively. It can be seen that the existing correlations can accurately reproduce the convective heat transfer behaviour of nanofluids in helically coiled tubes by adopting the measured properties of the nanofluids in the analysis. Based on the above experimental analysis, no anomalous heat transfer enhancement exists in either of the cases of laminar or turbulent flow.

According to eqs. (4.24) and (4.25), the heat transfer coefficient can only be enhanced by the same amount as the increase in thermal conductivity, assuming equal $Re^{0.775}Pr^{0.4}$ values for laminar flow and equal $Re^{0.85}Pr^{0.4}$ values for turbulent flow. The coil geometry is not considered here as the coil geometry was the same for all the experiments. As an example, Figs. 19 and 20 show the ratio of heat transfer coefficients of nanofluid to water, RH_{RePr}, for alumina/water nanofluid with a concentration of 7.04 wt. % and MWCNT/water nanofluid with a concentration of 0.10 wt. % for both laminar flow and turbulent flow, respectively. In general, RH_{RePr} is within the experimental error equal to the thermal conductivity ratio of respective nanofluid to water.

4.4. Annular counter flow heat exchanger (Aalto University, Finland)

Double pipe heat exchangers are of great practical relevance especially for high pressure and high temperature applications. They consist of an inner and an outer pipe. One of their advantages is that they can be operated in true counter flow regime. With the experiments provided by Aalto University (Finland) such a device is operated with alumina and silica nanofluids to test if their thermal performance can be further enhanced.

4.4.1. Description of test rig

Mikkola et al. [52,53] conducted convective heat transfer experiments using an annular counter flow (double pipe) heat exchanger (Fig. 21). The inner and outer tubes of the heat exchanger were 1470 mm long acid-resistant steel pipes with inner diameters of 6.0 mm and 13.00 mm, respectively. The thickness of inner pipe was 1.00 mm. Thus, the outer diameter of the inner pipe is 8.00 mm. The flow rates were controlled with pump frequency controllers. The heated nanofluid was arranged to flow upwards in the inner tube and the water flow in the external outer tube was set to flow downwards in the vertically positioned heat exchanger.

The temperatures of the fluids were measured with two K-type thermocouples (accuracy $\pm$ 0.05 K) at each inlet and outlet points. Before reaching the outlet thermocouples, the fluids were constricted in a narrow gap of 1.00 mm in diameter in order to ensure complete mixing of the fluid. The pressure losses were measured with a Yokogawa DP Harp pressure transmitter (accuracy 0.04%) over the test section within a distance of 1.68 m. The velocity of the working fluid was measured with an electromagnetic flow sensor (Optiflux 4000 IFC 300 signal converter, KROHNE Messtechnik GmbH and Co. KG, Germany, uncertainty 0.20%).

4.4.2. Preparation and characterization of nanofluid

Experiments were carried with 1.00 vol % alumina (Al_2O_3) and 0.09–1.81 vol % silica (SiO_2) nanofluid. The Al_2O_3 nanofluid was diluted from a commercial concentrated dispersion provided by Nanostructured & Amorphous Materials Inc. (USA). The nanoparticles employed for the SiO_2 nanofluid were self-synthesized employing Stöber's method [54] and then dispersed in water. Ion exchanged water
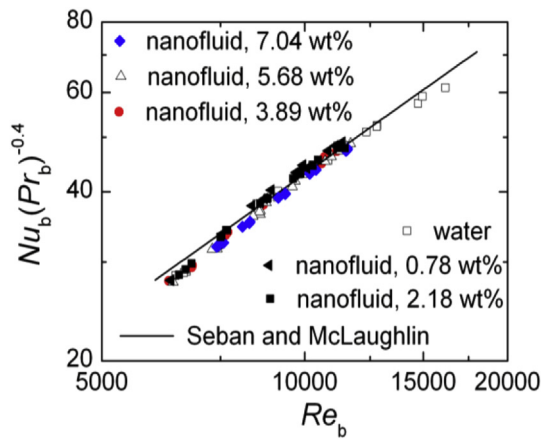
(a) Alumina nanofluid
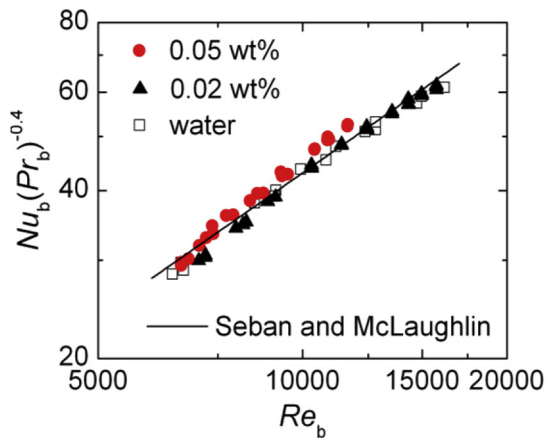
(b) MWCNT nanofluid

Fig. 18. $Nu_b(Pr_b)^{-0.4}$ vs. Re_b for turbulent flow against the Seban and McLaughlin [51] correlation (data from Refs. [49,50]).

was employed as base fluid for all samples.

Particle size distributions were determined with the dynamic light scattering (DLS) method employing the Malvern Zetasizer Nano ZS
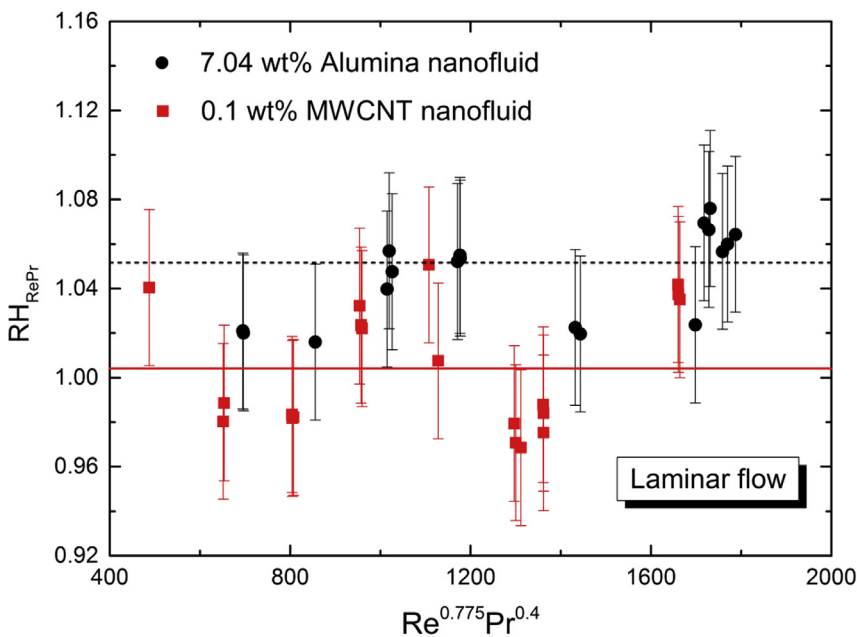

Fig. 20. Ratios of heat transfer coefficient for Re^mPr^n – scaling for turbulent flow. The full red line indicates increase of thermal conductivity for 0.10 wt. % MWCNT nanofluid and the broken line for 7.04 wt. % alumina nanofluid. (For interpretation of the references to colour in this figure legend, the reader is referred to the web version of this article.)

device with a reproducibility less than ± 5.00%. The mean nanoparticle size for Al_2O_3 nanofluid was 10.00 nm and for SiO_2 nanofluids between 47.00 and 58.00 nm. The polydispersity indices (PdI) of the distributions are given in Table 6. In addition, particle sizes of dried solid-particle nanofluid samples were verified with a Tecnai F-20 transmission electron microscope (TEM). The DLS measurements were conducted at temperatures of 25 °C and 60 °C in order to study the stability of the fluids in the temperature range used in the convective heat transfer measurements. The size distribution of each fluid was also verified with DLS after the convective heat transfer measurements. No significant differences were observed in particle size distributions measured at the two temperatures of 25 °C and 60 °C. It was found that all nanofluids remained unchanged also during the heat transfer measurements.

In addition to the particle size distributions, DLS was employed to determine zeta potentials of the nanofluids before the convective experiments. The zeta potentials reported for the fluids studied (Table 6) show relatively high absolute values indicating good resistance against
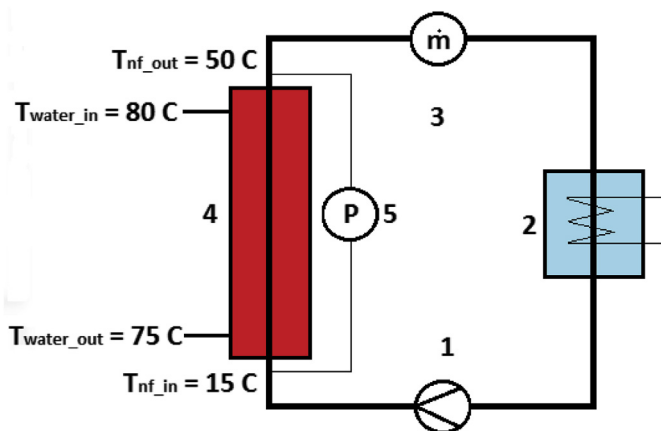
Fig. 19. Ratios of heat transfer coefficient for Re^mPr^n – scaling for laminar flow. The full red line indicates increase of thermal conductivity for 0.10 wt. % MWCNT nanofluid and the broken line for 7.04 wt. % alumina nanofluid. (For interpretation of the references to colour in this figure legend, the reader is referred to the web version of this article.)

Fig. 21. Schematic of the convection heat transfer measurement apparatus (annular counter flow heat exchanger): pump (1), cooler (2), flow meter (3), tube-in-tube type heat exchanger (4) and pressure meter (5).

Fig. 22. Experimentally determined viscosity of alumina and silica nanofluids with different concentrations for experiments in annular counter flow heat exchanger. Purple rhombi stand for SiO_2 NF with 0.09 vol %, orange squares for SiO_2 NF with 0.45 vol % and red dots for SiO_2 NF with 1.81 vol %. Dark yellow downward symbols indicate Al_2O_3 NF with 1.00 vol %. Bold curve shows viscosity of deionized water according to the NIST database [41]. Broken curves indicate the viscosity model according to Chevalier et al. [44]. (For interpretation of the references to colour in this figure legend, the reader is referred to the web version of this article.)

Table 6
The concentration (ϕ) and the main material properties of the nanofluids for annular counter flow heat exchanger. The particle size is measured with DLS and reported as the peak value of the number distribution. Values in parenthesis are measured 34 months after other property and convection measurements. Dynamic viscosity (η), thermal conductivity (k), density (ρ) and zeta potential (ζ) values are all measured at 25.00 °C.

Material of nanoparticles	ϕ (vol %)	Particle size (nm)	PdI	ζ (mV)	k_{nf}/k_{bf}	η_{nf}/η_{bf}	ρ_{nf}/ρ_{bf}
SiO_2	0.09	52 (51)	0.04 (0.04)	- 50.2	1.00	1.04	1.00
SiO_2	0.45	58 (52)	0.06 (0.10)	- 43.9	0.99	1.08	1.01
SiO_2	1.81	47 (43)	0.08 (0.09)	- 32.3	0.99	1.22	1.02
Al_2O_3	1.0	10 (14)	0.26 (0.22)	50.6	1.02	1.21	1.02

agglomeration. Zeta potential was measured at 20.00 °C and 60.00 °C.

All thermal property measurements were performed before the convection measurements. The viscosities of the alumina nanofluid were measured with a Haake falling ball type C viscometer (accuracy ± 0.50%) and the one of the silica nanofluids with a Brookfield DV3TLVCJ0 cone/plate rheometer (accuracy ± 1.50%) (Fig. 22). Based on repeated measurements, the maximum errors for these two measurement methods were estimated to be 0.50% and 1.50%, respectively. The temperature range in both viscosity measurements was 25 °C–60 °C. It was found that viscosity of the silica nanofluid coincides well with measurements of silica nanofluids of 2.00 vol % and 4.00 vol % carried out at ILK Dresden and Fraunhofer IKT Dresden [55]. For these measurements a rheometer MCR101 (Anton Paar) with a double gap system was employed.

A C-therm TCi-3-A thermal conductivity analyser was employed to measure the thermal conductivity at ambient temperature. The system is based on the modified transient source plane technique and has an accuracy of ± 3.00%. All the thermal conductivity measurements were carried out at the ambient temperature.

Densities of the nanofluids were determined using VWR Hydrometers (accuracy ± 0.10%). Specific heat capacities of the nanofluids $c_{p,nf}$ were calculated according to eq. (2.4). Values of specific heat of water (base fluid) and nanoparticles material were taken from Incropera and De Witt [56].

The measured zeta-potentials already indicated good stability of all nanofluids employed. In addition, the stability was tested by a 34 month aging period. As can be seen from Table 6, all fluids had
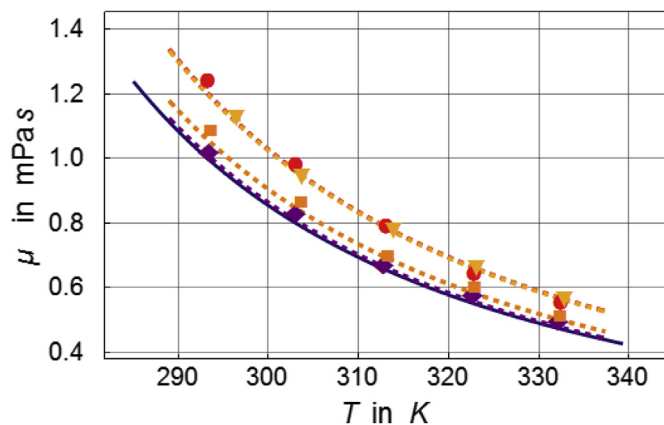
preserved their particle distributions well. Also, based on a visual inspection, no sedimentation occurred during these 34 months.

Because the structure of the fluids had stayed unaltered, it is clear that also all thermal and convective properties remained unchanged during the aging period.

4.4.3. Experimental procedure and error analysis

The temperature of the incoming nanofluid was set to 15.00–20.00 °C. The outlet temperature of the heated nanofluid varied between 45.00 °C and 78.00 °C, depending on the flow rate. The volumetric flow rate of the nanofluids varied in the range of 0.13–2.17 l/min.

Experimental heat transfer coefficients were determined based on the measured inlet and outlet temperatures, mass flows and fluid properties. The conductance G of the heat exchanger is defined as

$$G = \frac{\dot{m}c_p \Delta T}{LMTD}; \tag{4.27}$$

where $\dot{m}$ is the mass flow, c_p is the specific heat and ΔT the temperature change of the working fluid. $LMTD$ is calculated using eq. (4.20). Conductance per length can be also expressed as

$$\frac{1}{G/L} = \frac{1}{\pi d_i \overline{h}_i} + \frac{\ln\left(\frac{d_{io}}{d_i}\right)}{2\pi k_{tube}} + \frac{1}{\pi d_{io} \overline{h}_o}, \tag{4.28}$$

where $\overline{h}_i$ and $\overline{h}_o$ are the averaged inner and outer heat transfer coefficients, respectively, and k_{tube} the thermal conductivity of the tube (in this case, 15.00 W/mK). The heat transfer coefficient of nanofluid $\overline{h}_i$ can be calculated from eq. (4.28) after $\overline{h}_o$ is obtained using well-known correlations for the Nusselt number of turbulent flow. In this work, a method suggested by Petukhov and Roizen [57] for annular tube flow, is applied

$$\overline{Nu}_{ann} = \frac{\overline{h}_o d_h}{k} = 0.86 \, \overline{Nu}_{DB} \frac{d_o}{d_{io}}^{0.16}, \tag{4.29}$$

where the hydraulic diameter is $d_h = d_o - d_{io}$. Here $\overline{Nu}_{DB}$ denotes the Nusselt number according to the Dittus-Boelter correlation for cooling fluids of the external water side

$$\overline{Nu}_{DB} = 0.023 Re^{0.8} Pr^{0.3}, \tag{4.30}$$

where Re is the Reynolds number and Pr the Prandtl number of the hot

water flow. The hydraulic diameter d_h is used in the Reynolds number. Based on repeated measurements, the maximum experimental errors were estimated to be 2.00% for both heat transfer coefficients and pumping powers. The error in the reported value of Nusselt number and friction factor was estimated to be 5.00% and 3.00%, respectively.

4.4.4. Nusselt number correlation of reference fluid

A direct comparison between the experimental results and the Gnielinski correlation eq. (4.31) can be found in Kakaç et al. [58]. The correlation is valid in both the transitional and the turbulent pipe flow regimes and covers a Reynolds number range between 2,300 and 5×10^6:

$$\overline{Nu}_{cor} = \frac{\left(\frac{f}{2}\right)(Re - 1,000)Pr}{1 + 12.7\left(\frac{f}{2}\right)^{1/2}(Pr^{2/3} - 1)}.$$

(4.31)

The friction factor f is determined according Blasius correlation for turbulent pipe flow [59].

$$f = 0.316Re^{-0.25}; \quad (3 \times 10^3 < Re < 1 \times 10^5).$$

(4.32)

4.4.5. Experimental results of heat transfer and pressure loss

Experimental results for the Nusselt number are compiled in Fig. 23 (alumina) and Fig. 24 (silica). In both diagrams, the experimental Nusselt number is plotted versus the Nusselt number following from predicted heat transfer of annular counter flow heat exchanger based on the Gnielinski correlation (eq. (4.31)) For Nusselt numbers above 30 the experimental and predicted values coincide reasonably well. None of the experimental data depart more than about ± 5.00% from the predicted values. This is true both for pure base fluid and nanofluid flows. Below Nusselt numbers of about 30 the experimental results differ from the predicted ones. However, the experimental data for nanofluids as well as the base fluid still collapse on one single curve.

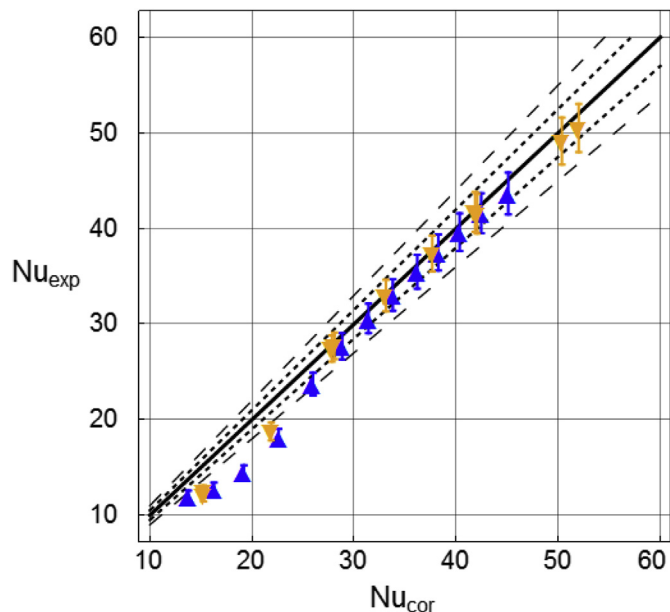The experimental friction factors over a wide range of Reynolds

Fig. 24. Experimentally determined Nusselt number for annular counter flow heat exchanger compared with Nusselt number predicted according to Gnielinski's equation for silica nanofluids. For symbols and lines, see Figs. 22 and 23.

numbers for both the pure base fluid and nanofluids are compiled in Fig. 25. Again data for the base fluid and nanofluid flow – alumina and silica – collapse to one curve. With increasing Reynolds number data of all fluids approach the Blasius correlation for turbulent pipe flow.

4.5. Flow in a plate heat exchanger (Lund University, Sweden)

Plate heat exchangers (PHEs) are widely used in many applications including food processing, heating and cooling applications and chemical industry for their high efficiency (high heat transfer coefficient) and compactness (low volume/surface ratio) [60]. The flow inside the narrow PHE channels may separate and reattach successively, creating strong turbulence and thus enhancing the heat transfer. In the literature, previous experimental work on nanofluids has mainly focused on simple flow geometries such as straight tubes, while investigations of nanofluids flowing in complex or enhanced geometries, i.e., coil heat exchangers and PHEs, are limited. This section will briefly present some of the experimental observations at Lund University (by Huang et al., [61]) regarding the heat transfer performances of Al_2O_3/water and

Fig. 23. Experimental Nusselt number for annular counter flow heat exchanger compared with Nusselt number predicted according to Gnielinski's equation for alumina nanofluids. Blue upright triangles indicate results for pure base fluid flow. For all other symbols see Fig. 22. Bold line indicates diagonal of plot and therewith accordance of both Nusselt numbers. Bold broken lines indicate error bars of 5.00% and bold thin lines those of 10.00%. (For interpretation of the references to colour in this figure legend, the reader is referred to the web version of this article.)
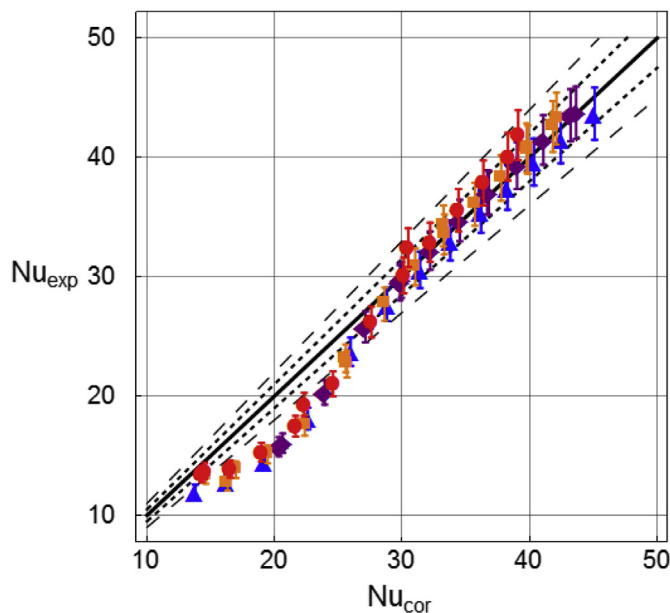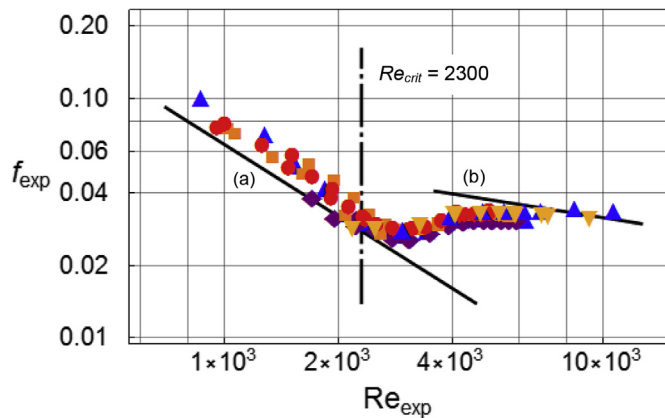
Fig. 25. Experimental friction factor of basefluid and nanofluid flow. For symbols, see Figs. 22 and 23. Line (a) indicates friction law for laminar pipe flow (64/Re) and line (b) is the Blasius correlation (eq. (4.32)).
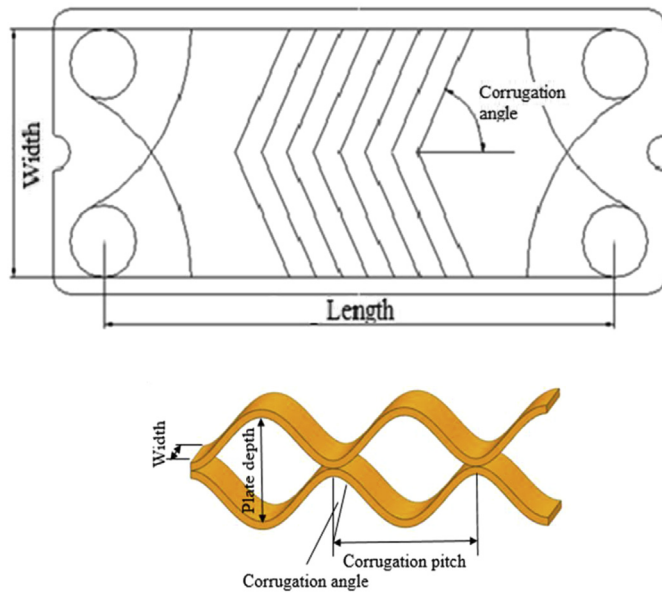
Fig. 26. Geometry of a corrugated plate in the tested PHE.

MWCNT/water nanofluids in a chevron brazed PHE.

4.5.1. Description of test rig

The same test rig as shown in Fig. 16 for the coil heat exchanger was used for experiments for the brazed PHE (see Sec. 4.3.1 for detailed description). The main difference in this test rig is that the coil heat exchanger was replaced by the brazed PHE. The brazed PHE was provided by Alfa Laval and consists of 20 stainless-steel corrugated plates, creating 10 flow channels for the hot fluid and 9 flow channels for the cold fluid, respectively. The plates are chevron-type with a plate depth of 4.00 mm and a corrugation pitch of 6.00 mm as shown in Fig. 26. The corrugation angle is 60.00°, which is defined as the angle between the corrugation and the axis parallel to the plate length. The detailed geometrical parameters of the PHE tested are listed in Table 7. The PHE was thermally insulated to reduce heat losses to the ambient. Water or nanofluid was chosen as the hot fluid flowing in a closed loop. The cold water flows counter-currently as the cold fluid in an open loop.

4.5.2. Preparation and characterization of nanofluids

The same procedures for preparation and characterization of nanofluids as described in Section 4.3.2 were used. Please refer to Section 4.3.2 for more details.

4.5.3. Data reduction and error analysis

The heat removed from the hot fluid Q_h and absorbed by the cold water Q_c were calculated by eqs. (4.33) and (4.34), respectively. Q_h and Q_c were supposed to be equal, while in the present study, the deviation between Q_h and Q_c was less than 5.00%. The overall heat transfer rate, Q, was taken to be the average:

Table 7
Detailed geometrical parameters of the plate heat exchanger.

Parameters	Value
plate length, L	150.00 mm
plate width, w	70.00 mm
plate depth, $2b_p$	4.00 mm
plate thickness, δ	0.30 mm
heat transfer area per plate	0.013 m²
corrugation pitch	6.00 mm
corrugation angle	60.00°
surface enlargement ratio	1.2375

$$Q_h = m_h c_{p,h} (T_{hi} - T_{ho});\tag{4.33}$$

$$Q_c = m_c c_{p,c} (T_{co} - T_{ci});\tag{4.34}$$

$$Q = (Q_h + Q_c)/2.\tag{4.35}$$

The total heat transfer coefficient, U, was calculated using eq. (4.36) based on the averaged heat amount Q, the total heat transfer area A, which is 0.234 m², and the log mean temperature difference $LMTD$ (for definition of $LMTD$ see eq. (4.20)):

$$U = \frac{Q}{A \cdot LMTD}\tag{4.36}$$

The heat transfer coefficient of the hot fluid side can be calculated by:

$$\frac{1}{U} = \frac{1}{h_c} + \frac{\delta}{\lambda_{plate}} + \frac{1}{h_h}.\tag{4.37}$$

where δ is the plate thickness equal to 0.30 mm, λ_{plate} is the plate's thermal conductivity which is 14.10 W/mK at 20 °C and 15.40 W/mK at 100 °C.

In order to get the heat transfer coefficient of the hot fluid (h_h), the heat transfer coefficient of the cold fluid (cold water, h_c) is needed. It is generally accepted that the following correlation can be used to predict the heat transfer coefficient of fluids in PHEs:

$$Nu = a\, Re_e^{\,b}\, Pr^c,\tag{4.38}$$

where Re_e can be calculated based on the average bulk temperature $T_{ave} = (T_i + T_o)/2$ and the equivalent diameter D_e defined as the plate depth 2 b_p. The exponent c is supposed to be 0.30 for the hot fluid and 0.40 for the cold fluid.

In order to identify the value of the constants (i.e. a and b), experiments were carried out with water both for the hot and the cold side. Because the working fluid and the plate geometry were the same, the constants a and b in eq. (4.38) should be the same for hot and cold water in the same flow regime.

First, the total heat transfer coefficient could be readily obtained by eq. (4.37) and the first guess of the heat transfer coefficient for the cold side ($h_{c,w}$) can be obtained by using the following correlation proposed by Martin [62]:

$$Nu = 1.615[f\,(Re/64)RePrD_h/L]^{1/3}\tag{4.39}$$

where Re is the Reynolds number based on the hydraulic diameter and defined as $D_h = 2b_p/\Phi$, where Φ is the surface enlargement ratio (ratio of the actual corrugated surface area to its projected area) and f is the friction factor related to the corrugation angle of PHE and the Reynolds number [62].

Next the heat transfer coefficient of the hot side ($h_{h,w}$) and the Nusselt number can be obtained by using eqs. (4.37) and (4.38). By plotting the relationship between $Nu_h/Pr_h^{0.3}$ and Re_h, the constants a and b were identified. The a and b values were then substituted back into the correlation $Nu_c = a\, Re_c^b Pr_c^{0.4}$ to get a new value of $h_{c,w}$. This new value of the cold side heat transfer coefficient, $h_{c,w}$, can be inserted again in eqs. (4.36) and (4.37) to find a new value of heat transfer coefficient on the hot side, $h_{h,w}$. New values of a and b can be obtained by plotting the relationship between $Nu_h/Pr_h^{0.3}$ and Re_h. This algorithm was repeated until a sufficiently small difference was observed between the new and old values of a and b. Finally, the correlation used to calculate the heat transfer coefficient of cold water is obtained as $Nu = 0.3762\ Re_e^{0.6681}Pr^{0.4}$, where the Reynolds number range is $40 < Re_e < 630$.

The propagated uncertainties of h, Nu and Pr of the hot side are 5.40%, 6.20% and 4.20%, respectively. All properties used in the dimensionless numbers were calculated at the average bulk fluid temperature which was estimated from the hot-side inlet and outlet temperatures.
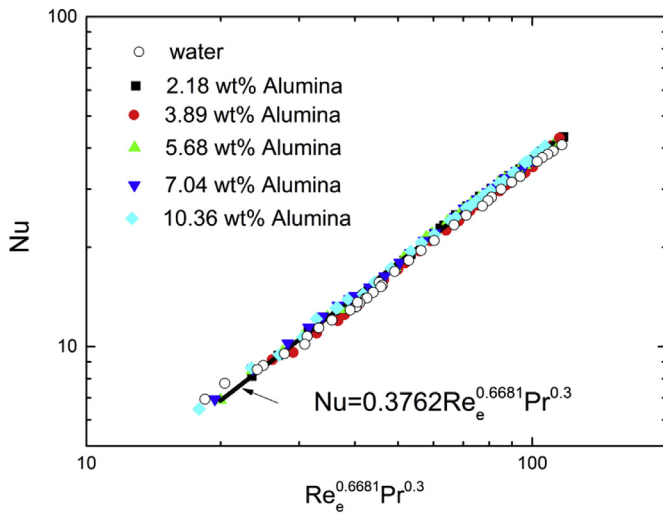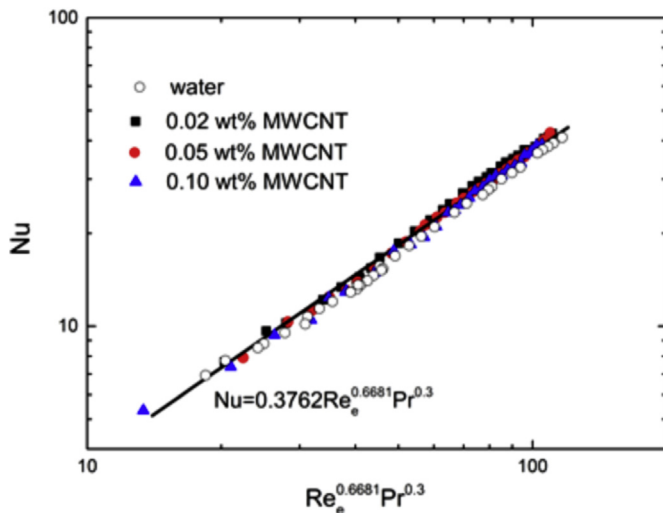
Fig. 27. Nusselt number vs. $Re_e^{0.6681}Pr^{0.3}$ for water and alumina/water nanofluids for plate heat exchanger. The black line indicates the Huang et al. [63] correlation.

4.5.4. Nusselt number correlation of the reference fluid

The Nusselt number correlation of the reference fluid, i.e., water, flowing in the hot side of the tested PHE is given by Huang et al. [63]:

$$Nu = 0.3762 \, Re_e^{0.6681}Pr^{0.3}. \tag{4.40}$$

The equivalent diameter is used as the characteristic length in the dimensionless numbers. The applicable range of the correlation is $40 < Re_e < 630$ and $4.50 < Pr < 7.00$.

4.5.5. Experimental heat transfer results for nanofluids

As shown in Figs. 27 and 28, alumina nanofluids with five different concentrations and MWCNT nanofluids with three different concentrations show trends very similar to water. Nanofluid properties measured at the average bulk temperature were used to calculate the dimensionless numbers. The Nu increases linearly with $Re_e^{0.6681}Pr^{0.3}$ for water and nanofluids. A perfect collapse of all the water and nanofluid data is achieved with eq. (4.40). In other words, in agreement to the previous sections, when the measured nanofluid properties are used in the analysis, all the water and nanofluid data can be well predicted by

Fig. 28. Nusselt number vs. $Re_e^{0.6681}Pr^{0.3}$ for water and MWCNT/water nanofluids for plate heat exchanger. The black line indicates the Huang et al. [63] correlation.
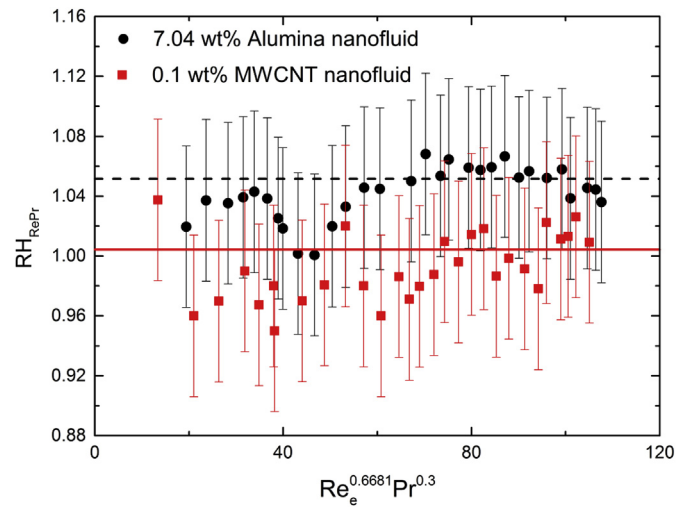

Fig. 29. Ratios of heat transfer coefficient for Re^mPr^n – scaling for nanofluid flowing in the PHE. The full red line indicates increase of thermal conductivity for 0.10 wt. % MWCNT nanofluid and the broken line for 7.04 wt. % alumina nanofluid. (For interpretation of the references to colour in this figure legend, the reader is referred to the web version of this article.)

the same correlation which is independent of the nanoparticle concentration. No additional nanofluid parameters are needed to evaluate the heat transfer performance of the nanofluids.

According to eq. (4.40), at constant value of the Reynolds and the Prandtl numbers, the heat transfer coefficient can only be enhanced by the same amount as the increase in thermal conductivity. The plate geometry of the PHE is not considered here as the same PHE was employed for different working fluids. As an example, Fig. 29 shows the ratio of the heat transfer coefficient of nanofluid to water, RH_{RePr}, for alumina/water nanofluid with a concentration of 7.04 wt. % and MWCNT/water nanofluid with a concentration of 0.10 wt. %. In general, RH_{RePr} is within experimental error equal to the thermal conductivity ratio of nanofluid to water. No anomalous heat transfer enhancement was observed in these cases.

5. Conclusion

In this study, an extensive concentrated effort has been made to clear up some of the common misconceptions regarding nanofluid convective heat transfer interpretations. The main question that this study has tried to answer was whether or not nanofluids can be treated as homogeneous fluids.

To answer this question, this study has summarized the observations from five different research groups, which worked on various experiments using standard heat transfer apparatus commonly employed in industrial applications.

Based on the experiments presented here and a profound similarity analyses, the following conclusions are drawn:

1. Newtonian nanofluid flow is sufficiently described employing Nusselt number correlations obtained for single-phase heat transfer liquids such as water when thermophysical properties of nanofluid are utilized. No anomalous phenomena are involved in thermal conduction based and forced convection heat transfer of nanofluids. Therefore, Newtonian nanofluids can be treated as homogeneous fluids in the most cases.

2. Heat transfer enhancement provided by nanofluids equals the increase in thermal conductivity of nanofluids compared to base fluid, if similar thermodynamical and fluid mechanical flows (i.e., same Re and Pr numbers) are compared. This observation was independent of nanoparticle concentration, size or material.

3. Statements 1 and 2 are true for several industrial relevant heat transfer apparatus.

Based on the results of this study, potential guidelines for evaluating nanofluid performance in heat transfer applications can be laid out as follows:

a) The first step is to identify if the nanofluid of interest shows Newtonian behaviour or not. If the nanofluid of interest is non-Newtonian then this method of evaluation does not apply.
b) The second step is to measure the thermal conductivity and viscosity of nanofluid at the concentration of interest and in the temperatures interval relevant for the application. As mentioned earlier, nanofluid literature provides some correlations for thermal conductivity and viscosity of nanofluids, however, taking measurements for a specific nanofluid is a much more reliable method at this stage.
c) Next, calculate density and specific heat of the nanofluid using eqs. (2.3) and (2.4).
d) Finally, implement these measured/calculated thermophysical properties of the specific nanofluid in traditional correlations developed for convective heat transfer and pressure drop of single-phase liquids.

To summarize, dilute, water based nanofluids such as investigated with this study can be treated as homogeneous fluids and may indeed be an option to increase heat transfer. However, the interpretation of physical phenomena relevant and therewith the data obtained in experiments have to be done properly. There are no anomalous or unexplainable effects. Following our study the main task is to produce nanofluids with a high thermal conductivity and the lowest possible viscosity.

Appendix

Appendix A
Non-dimensionalisation of conservation of mass, momentum, and thermal energy equation

$$x_j = \frac{x_j^*}{L_{bf,R}^*} \qquad \tau = \frac{t^*}{L_{bf,R}^* / u_{bf,R}^*}$$

$$u_j = \frac{u_j^*}{u_{bf,R}^*} \qquad \Theta = \frac{T^*}{T_{bf,R}^*} \qquad p = \frac{p^*}{\left(\rho_{np,R}^* - \rho_{bf,R}^*\right) u_{bf,R}^{*2}}$$

$$\rho_{bf} = \frac{\rho_{bf}^*}{\rho_{np,R}^* - \rho_{bf,R}^*} \qquad c_{p,bf} = \frac{c_{p,bf}^*}{c_{p,bf,R}^* - c_{p,np,R}^*}$$

$$k_{bf} = \frac{k_{bf}^*}{k_{np,R}^* - k_{bf,R}^*} \qquad \mu_{bf} = \frac{\mu_{bf}^*}{\mu_{bf,R}^*}$$

$$D_{B,R} = \frac{D_B^*}{D_{B,R}^*} \qquad D_{T,R} = \frac{D_T^*}{D_{T,R}^*}$$

$$\Phi \underline{\underline{def}} \frac{\rho_{nf}^* - \rho_{bf,R}^*}{\rho_{np,R}^* - \rho_{bf,R}^*} \qquad q_w = \frac{q_{BwT}^*}{q_{w,R}^*}$$

Appendix B
Non-dimensionalisation of heat equation

$$x_j = \frac{x_j^*}{L_{np,R}^*} \qquad \tau = \frac{t^*}{\tau_R^*} \qquad \Theta = \frac{T_{np}^*}{T_{np,R}^*}$$

$$\rho_{np} = \frac{\rho_{np}^*}{\rho_{np,R}^*} \qquad c_{p,np} = \frac{c_{p,np}^*}{c_{p,np,R}^*} \qquad k_{np} = \frac{k_{np}^*}{k_{np,R}^*}$$

References

[1] D. Wen, Y. Ding, Effect of particle migration on heat transfer in suspensions of nanoparticles flowing through minichannels, Microfluid Nanofluidics 1 (2005) 183–189, http://dx.doi.org/10.1007/s10404-004-0027-2.

[2] D.C. Venerus, J. Buongiorno, R. Christianson, et al., Viscosity measurements on colloidal dispersions (nanofluids) for heat transfer applications, Appl Rheol 20

(2010) 44582 http://doi.org/10.3933/ApplRheol-20-44582.

[3] J. Buongiorno, D.C. Venerus, N. Prabhat, et al., A benchmark study on the thermal conductivity of nanofluids, J Appl Phys 106 (2009) 094312 https://doi.org/10.1063/1.3245330.

[4] A. Einstein, Eine neue Bestimmung der Moleküldimensionen, Ann Phys 19 (1906) 289.

[5] L.P. Zhou, B.X. Wang, X.F. Peng, X.Z. Du, Y.P. Yang, On the specific heat capacity of CuO nanofluid, Adv Mech Eng (2010) 172085.

[6] H. O'Hanely, J. Buongiorno, T. McKrell, L.-W. Hu, Measurement and model validation of nanofluid specific heat capacity with differential scanning calorimetry, Adv Mech Eng (2012) 181079.

[7] D. Wen, Y. Ding, Experimental investigation into convective heat transfer of nanofluids at the entrance region under laminar flow conditions, Int J Heat Mass Transf 47 (2004) 5181–5188, http://dx.doi.org/10.1016/j.ijheatmasstransfer.2004.07.012.

[8] Y. Ding, H. Alias, D. Wen, R.A. Williams, Heat transfer of aqueous suspensions of carbon nanotubes (CNT nanofluids), Int J Heat Mass Transf 49 (2006) 240–250, http://dx.doi.org/10.1016/j.ijheatmasstransfer.2005.07.009.

[9] S.Z. Heris, M.N. Esfahany, G. Etemad, Investigation of CuO/water nanofluid laminar convective heat transfer through a circular tube, J Enhanc Heat Transf 13 (2006) 279–289, http://dx.doi.org/10.1016/j.ijheatmasstransfer.2006.01.005.

[10] U. Rea, T. McKrell, L.W. Hu, J. Buongiorno, Laminar convective heat transfer and viscous pressure loss of alumina-water and zirconia-water nanofluids, Int J Heat Mass Transf 52 (2009) 2042–2048, http://dx.doi.org/10.1016/j.ijheatmasstransfer.2008.10.025.

[11] R. Azizian, E. Doroodchi, T. McKrell, J. Buongiorno, L.W. Hu, B. Moghtaderi, Effect of magnetic field on laminar convective heat transfer of magnetite nanofluids, Int J Heat Mass Transf 68 (2014) 94–109 https://doi.org/10.1016/j.ijheatmasstransfer.2013.09.011.

[12] W.C. Williams, J. Buongiorno, L.W. Hu, Experimental investigation of turbulent convective heat transfer and pressure loss of alumina/water and zirconia/water nanoparticle colloids (nanofluids) in horizontal tubes, J Heat Transf 130 (2008) 042412, http://dx.doi.org/10.1115/1.2818775.

[13] S. Pohl, S. Feja, M.H. Buschmann, Thermal conductivity and heat transfer of ceramic nanofluids show classical behaviour, International Symposium on thermal and materials nanoscience and nanotechnology, May 29-June 3, 2011 Antalya, Turkey.

[14] M.H. Buschmann, S. Feja, Nanofluids – potentials and illusions, WIT Trans Eng Sci 75 (2012) 195–205, http://dx.doi.org/10.2495/HT120171.

[15] M. Gad-el-Hak, Transport phenomena in microdevices, Z Ang Math Mech 84 (2004) 494–498 https://doi.org/10.1002/zamm.200310118.

[16] M.C. Ruzicka, On dimensionless numbers, Chem Eng Res Des 86 (2008) 835–868 https://doi.org/10.1016/j.cherd.2008.03.007.

[17] A. Prosperetti, G. Tryggvason, Computational methods for multiphase flow, Cambridge University Press, 2007.

[18] C. Yang, W. Li, Y. Sano, M. Mochizuki, On the anomalous convective heat transfer enhancement in nanofluids: a theoretical answer to the nanofluids controversy, Heat Transf ASME 135 (2013) 054504–1–9 https://doi.org/10.1115/1.4023539.

[19] J. Buongiorno, Convective transport in nanofluids, Heat Transf ASME 128 (2006) 240–250 https://doi.org/10.1115/1.2150834.

[20] K. Gersten, H. Herwig, Strömungsmechanik, Verlag Vieweg, 1992.

[21] J. Eapen, R. Rusconi, R. Piazza, S. Yip, The classical nature of thermal conduction in nanofluids, Heat Transf ASME 132 (2010) 102402–102402-14 https://doi.org/10.1115/1.4001304.

[22] G. Dewitt, T. McKrell, J. Buongiorno, L.-W. Hu, R.J. Park, Experimental study of critical heat flux with alumina-water nanofluids in downward-facing channels for in-vessel retention applications, Nucl Eng Technol 45 (3) (2012) 335–346.

[23] S.J. Kim, I.C. Bang, J. Buongiorno, L.W. Hu, Effects of nanoparticle deposition on surface wettability influencing boiling heat transfer in nanofluids, Appl Phys Lett 89 (2006) 153107, , http://dx.doi.org/10.1063/1.2360892.

[24] R. Martínez-Cuenca, R. Mondragón, L. Hernández, C. Segarra, J.C. Jarque, T. Hibiki, et al., Forced-convective heat-transfer coefficient and pressure drop of water-based nanofluids in a horizontal pipe, Appl Therm Eng 98 (2016) 841–849 https://doi.org/10.1016/j.applthermaleng.2015.11.050.

[25] W. Duangthongsuk, S. Wongwises, An experimental study on the heat transfer performance and pressure drop of tio2-water nanofluids flowing under a turbulent flow regime, Int J Heat Mass Transf 53 (1) (2010) 334–344, http://dx.doi.org/10.1016/j.ijheatmasstransfer.2009.09.024.

[26] M. Corcione, M. Cianfrini, A. Quintino, Heat transfer of nanofluids in turbulent pipe flow, Int J Therm Sci 56 (2012) 2012, http://doi.org/10.1016/j.ijthermalsci.2012.01.009.

[27] W. Yu, D. France, D. Smith, D. Singh, E. Timofeeva, J. Routbort, Heat transfer to a silicon carbide/water nanofluids, Int J Heat Mass Transf 52 (2009) 3606–3612, http://dx.doi.org/10.1016/j.ijheatmasstransfer.2009.02.036.

[28] B. Pak, Y. Cho, Hydrodynamic and heat transfer study of dispersed fluids with submicron metallic oxide particles, Exp Heat Transf 11 (1998) 151–170, http://dx.doi.org/10.1080/08916159808946559.

[29] A. Merilainen, A. Seppälä, K. Saari, J. Seitsonen, J. Ruokolainen, S. Puisto, et al., Effect of particle size and shape on turbulent heat transfer characteristics and pressure losses in water-based nanofluids, Int J Heat Mass Transf 61 (2013) 439–448, http://dx.doi.org/10.1016/j.ijheatmasstransfer.2013.02.032.

[30] S. Torii, Turbulent heat transfer behaviour of nanofluid in a circular tube heated under constant heat flux, Adv Mech Eng 2010 (2010) 917612, http://dx.doi.org/10.1155/2010/917612.

[31] S. Ferrouillat, A. Bontemps, J.P. Ribeirob, J. Gruss, O. Soriano, Hydraulic and heat transfer study of sio2/water nanofluids in horizontal tubes with imposed wall temperature boundary conditions, Int J Heat Fluid Flow 32 (2011) 424–439 https://doi.org/10.1016/j.applthermaleng.2012.10.020.

[32] N. Prabhat, J. Buongiorno, L.-H. Lin-Wen Hu, Convective heat transfer enhancement in nanofluids: real anomaly or analysis artefact? J Nanofluids 1 (2012) 55–62.

[33] M. Heyhat, F. Kowsary, A. Rashidi, S. Esfehani, A.G. Amrollahi, Experimental investigation of turbulent flow and convective heat transfer characteristics of alumina water nanofluids in fully developed flow regime, Int. Commun, Heat Mass Transf 39 (8) (2012) 1272–1278, http://dx.doi.org/10.1016/j.icheatmasstransfer .2012.06.024.

[34] M. Kayhani, H. Soltanzadeh, M. Heyhat, M. Nazari, F. Kowsary, Experimental study of convective heat transfer and pressure drop of tio2/water nanofluid, Int Commun Heat Mass Transf 39 (2012) 456–462, http://dx.doi.org/10.1016/j.icheatmasstransfer.2012.01.004.

[35] W.C. Williams, Experimental and theoretical investigation of transport phenomena in nanoparticle colloids (nanofluids), Ph.D. Thesis Massachusetts Institute of Technology, Cambridge, 2007.

[36] R. Rusconi, W.C. Williams, J. Buongiorno, R. Piazza, L.W. Hu, Numerical analysis of convective instabilities in a transient short-hot-wire setup for measurement of liquid thermal conductivity, J Thermophys 28 (2007) 1131–1146.

[37] J.H. Lienhard IV, J.H. Lienhard V, A heat transfer textbook, second ed., Phlogiston Press, 2002.

[38] A.E. Bergles, Recent developments in enhanced heat transfer, Heat Mass Transf 47 (2011) 1001–1008, http://dx.doi.org/10.1007/s00231-011-0872-y.

[39] M.H. Buschmann, Nanofluid heat transfer in laminar pipe flow with twisted tape, Heat Transf Eng 38 (2017) 162–176, http://dx.doi.org/10.1080/01457632.2016.1177381.

[40] EVONIK Degussa GmbH, product information AERODISP-W-740-X-EN.pdf http://www.aerosil.com/www2/uploads/productfinder/AERODISP-W-740-X-EN.pdf. [retrieved October 2015].

[41] See the NIST Reference Fluid Thermodynamic and Transport Properties Database (REFPROP), available online at http://www.nist.gov/srd/nist23.cfm [retrieved June 2007].

[42] A. Ehle, S. Feja, M.H. Buschmann, Temperature dependency of ceramic nano-fluids shows classical behaviour, J Thermophys Heat Transf 25 (2011) 378–385, http://dx.doi.org/10.2514/1.T3634.

[43] M.H. Buschmann, Thermal conductivity and heat transfer of ceramic nanofluids, Int J Therm Sci 62 (2012) 19–28, http://dx.doi.org/10.1016/j.ijthermalsci.2011.09.019.

[44] J. Chevalier, O. Tillement, F. Ayela, Structure and rheology of SiO$_2$ nanoparticle suspensions under very high shear rates, Phys Rev E 80 (2009), http://dx.doi.org/10.1103/PhysRevE.80.051403 051403–1–051403-7.

[45] R.M. Manglik, A.E. Bergles, Heat transfer and pressure drop correlations for twisted-tape inserts in Isothermal tubes: Part II - laminar flows, J Heat Transf 115 (1993) 881–889, http://dx.doi.org/10.1115/1.2911383.

[46] R.M. Manglik, A.E. Bergles, Heat transfer and pressure drop correlations for twisted-tape inserts in Isothermal tubes: Part II - turbulent flows, J Heat Transf 115 (1993) 881–889, http://dx.doi.org/10.1115/1.2911384.

[47] R.M. Manglik, A.E. Bergles, Swirl flow heat transfer and pressure drop with twisted-tape inserts, Adv Heat Transf 36 (2002) 183–263 ISBN 0-12-020036-8.

[48] Y. Mori, W. Nakayama, Study on forced convective heat transfer in curved pipes, Int J Heat Mass Transf 8 (1965) 67–82 https://doi.org/10.1016/0017-9310(65)90098-0.

[49] Z. Wu, L. Wang, B. Sundén, Pressure drop and convective heat transfer of water and nanofluids in a double-pipe helically coiled heat exchanger, Appl Therm Eng 60 (2013) 266–274 https://doi.org/10.1016/j.applthermaleng. 2013.06.051.

[50] Z. Wu, L. Wang, B. Sundén, L. Wadsö, Aqueous carbon nanotube nanofluids and their thermal performance in a helical heat exchanger, Appl Therm Eng 96 (2016) 364–371 https://doi.org/10.1016/j.applthermaleng.2014.10.096.

[51] R.A. Seban, E.F. McLaughlin, Heat transfer in tube coils with laminar and turbulent flow, Int J Heat Mass Transf 6 (1963) 387–395 Spain.

[52] V. Mikkola, S. Puupponen, H. Granbohm, K. Saari, T. Ala-Nissilä, A. Seppälä, Convective heat transfer performance of polystyrene, SiO$_2$, Al$_2$O$_3$ and micelle nanofluids, Proc HEFAT2016 (July 2016) 11–13 Spain.

[53] V. Mikkola, S. Puupponen, H. Granbohm, K. Saari, T. Ala-Nissilä, A. Seppälä, Influence of particle properties on convective heat transfer of nanofluids, Int J Therm Sci 124 (2018) 187–195.

[54] W. Stöber, A. Fink, E. Bohn, Controlled growth of monodisperse silica spheres in the micron range, J Colloid Interface Sci 26 (1968) 62, http://dx.doi.org/10.1016/0021-9797(68)90272-5.

[55] M. H. Buschmann Private correspondence (2017)..

[56] F.P. Incropera, D.P. De Witt, Fundamentals of heat and mass transfer, third ed., John Wiley & Sons, Inc, 0-471-51729-1, 1990.

[57] Y.A. Cengel, Heat transfer - a practical approach, 2. Edition, McGraw-Hill, 0-07-115150-8, 2003.

[58] S. Kakaç, Y. Yener, A. Pramuanjaroenkij, Convective heat transfer, third ed., CRC Press, Taylor & Francis Group, 978-1-4665-8344-3, 2014.

[59] F.M. White, Viscous fluid flow, third ed., McGraw-Hill, 007-124493-X, 2006.

[60] L. Wang, B. Sundén, R.M. Manglik, Plate Heat exchangers: design, applications and performance, WIT Press, Southampton, UK, 2007.

[61] D. Huang, Z. Wu, B. Sundén, Pressure drop and convective heat transfer of Al$_2$O$_3$/water and MWCNT/water nanofluids in a chevron plate heat exchanger, Int J Heat Mass Transf 89 (2015) 620–626.

[62] H. Martin, A theoretical approach to predict the performance of chevron-type plate heat exchangers, Chem Eng Process 35 (1996) 301–310.

[63] D. Huang, Z. Wu, B. Sundén, Effects of hybrid nanofluid mixture in plate heat exchangers, Exp Therm Fluid Sci 72 (2016) 190–196.

[64] H. Herwig, Wärmeübertragung A-Z, Springer-Verlag Berlin Heidelberg GmbH, 2000.

[65] Product information of AERODISP®W740X https://www.aerosil.com/www2/uploads/-productfinder/AERODISP-W-740-X-EN.pdf [retrieved 2017-09-12].

[66] H. Setia, R. Gupta, R.K. Wanchoo, Stability of nanofluids, Mater Sci Forum 757 (2013) 139–149 10.4028/www.scientific.net/MSF.757.139.

[67] Y. Hwang, J.K. Lee, C.H. Lee, Y.M. Jung, S.I. Cheong, C.G. Lee, et al., Stability and thermal conductivity characteristics of nanofluids, Thermochim Acta 455 (2007) 70–74, http://dx.doi.org/10.1016/j.tca.2006.11.036.

[68] R. Mondragón, C. Segarra, R. Martínez-Cuenca, J.E. Juliá, J.C. Jarque, Experimental characterization and modelling of thermophysical properties of nanofluids at high temperature conditions for heat transfer applications, Powder Technol 249 (2013) 516–529 https://doi.org/10.1016/j.powtec.2013.08.035.